

RHESSI Timing Studies: I. Thermal Delays

Markus J. Aschwanden

*Lockheed Martin Advanced Technology Center, Solar & Astrophysics Laboratory, Org. ADBS, Bldg.252,
3251 Hanover St., Palo Alto, CA 94304, USA; e-mail: aschwanden@lmsal.com*

ABSTRACT

We investigate the energy-dependent timing of thermal emission in solar flares, using high-resolution spectra and demodulated time profiles from the RHESSI instrument. We model for the first time the spectral-temporal hard X-ray flux $f(\epsilon, t)$ in terms of a multi-temperature plasma governed by thermal conduction cooling. In this quantitative model we characterize the multi-temperature differential emission measure distribution (DEM), the nonthermal spectra, the scaling of flare density, volume, and loop length as a function of temperature with powerlaw functions. We fit this model to the spectra and energy-dependent time delays of a representative dataset of 89 solar flares observed with RHESSI during 2002-2005. Eliminating weak flares we find 65 events suitable for fitting and obtain in 44 events (68%) a satisfactory fit that is consistent with the theoretical model. The best-fit results yield a thermal-nonthermal cross-over energy of $\epsilon_{th} = 18.0 \pm 3.4$ keV, nonthermal spectral indices of $\gamma_{nth} = 3.5 \pm 1.1$ (at ≈ 30 -50 keV), thermal multi-spectral indices of $\gamma_{th} = 6.9 \pm 0.09$ (at ≈ 10 -20 keV), thermal conduction cooling times of $\tau_{c0} = 10^{1.6 \pm 0.6}$ s at $\epsilon_{th} = 1$ keV (or $T_0 = 11.6$ MK), which scale with temperature as $\tau_c(T) \propto T^{-\beta}$ with $\beta = 2.7 \pm 1.2$, consistent with the theoretically expected scaling of $\tau_c(T) \propto T^{-5/2}$ for thermal conduction cooling. The (empirical) Neupert effect is consistent with this theoretical model in the asymptotic limit of long cooling times. This study provides clear evidence that all analyzed flares are consistent with the model of a multi-temperature plasma distribution and with thermal conduction as dominant cooling mechanism (at flare temperatures of $T \gtrsim 10$ MK). We demonstrate that this method of modeling energy-dependent time delays provides a powerful tool to separate thermal from nonthermal spectral components, which is not achievable by spectral-fitting alone.

Subject headings: Flares — Hard X-rays

1. INTRODUCTION

The analysis of energy-dependent time delays permits us to test theoretical models of physical time scales and their scaling laws with energy. In the wavelength domain of hard X-rays there are at least three physical processes known in the observation of solar flares that lead to measurable time delays as a function of energy (for a review see, e.g., Aschwanden 2004): (1) time-of-flight dispersion of free-streaming electrons, (2) collisional trapping of electrons, and (3) the Neupert effect. Time-of-flight delays have a scaling of $\Delta t(\epsilon) \propto \epsilon^{-1/2}$ and are caused by velocity differences of electrons that propagate from the coronal acceleration site to the chromospheric energy-loss region, observable as tiny time differences of order $\Delta t \approx 0.01 - 0.1$ s for nonthermal electrons at energies of $\epsilon \approx 20 - 100$ keV (e.g., Aschwanden, Schwartz, & Alt 1995; Aschwanden et al. 1996). Trapping delays are caused by magnetic mirroring of

coronal electrons which precipitate towards the chromosphere after a collisional time scale, which has the scaling of $\Delta t(\epsilon) \propto \epsilon^{3/2}$ and are observable from time differences of $\Delta t \approx 1 - 10$ s for nonthermal electrons of $\epsilon \approx 20 - 100$ keV (e.g., Vilmer, Kane, & Trotter 1982; Aschwanden et al. 1997); Thermal delays can be caused by the temperature dependence of cooling processes, such as thermal conduction, $\tau_c(T) \propto T^{-5/2}$ (e.g., Antiochos & Sturrock 1978; Culhane et al. 1994), or radiative cooling, $\tau_r(T) \propto T^{5/3}$ (e.g., Fisher & Hawley 1990; Cargill et al. 1995). The observed physical parameters suggest that thermal conduction dominates in flare loops at high temperatures as observed in soft X-ray wavelengths, while radiative cooling dominates in the later phase of cooling in postflare loops as observed in EUV wavelengths (Antiochos & Sturrock 1978; Culhane et al. 1994; Aschwanden & Alexander 2001). In several flares the cooling curve $T(t)$ has been inferred for cooling flare plasmas in different temperature filters or wavelength bands (e.g., Culhane et al. 1994; Aschwanden & Alexander 2001), but no study has been conducted yet by using RHESSI time profiles with unprecedented high resolution in the spectral domain, which translates into a large number of independent “temperature filters”.

The high spectral resolution of RHESSI data is particularly suitable for any type of thermal modeling, because we can probe the thermal plasma from ≈ 3 keV up to ≈ 30 keV with a resolution of $\gtrsim 1$ keV thanks to the cooled germanium detectors (Lin et al. 2002). This allows us to measure flare temperatures with more confidence, and a statistical study of flare temperatures measured in the range of $T \approx 7 - 20$ MK indeed demonstrates excellent agreement between the values obtained from spectral fitting of RHESSI data with those obtained from flux ratios with GOES (Battaglia et al. 2005). An intimate relationship between the nonthermal and thermal time profiles has been found early on, in the sense that the thermal emission resembles often close to the integral of the nonthermal emission, which has been dubbed the *Neupert effect* (Hudson 1991; Dennis & Zarro 1993). This is, however, strictly true only for the asymptotic limit of very long cooling times, while a physically more accurate model would quantify this effect by a convolution of the nonthermal emission with a finite cooling time. The deconvolution of the e-folding cooling time in such a model has never been attempted systematically for a larger sample and as a function of energy or temperature. A cooling time at a given energy can be estimated from the decay times in flare time profiles, e.g., the decay times measured with GOES in soft X-rays were found to have a median of $\tau_{decay} \approx 6$ min (Veronig et al. 2002a,c). The Neupert effect was tested by correlating the soft X-ray peak flux with the (time-integrated) hard X-ray fluence. A high correlation and time coincidence between the soft X-ray peak and hard X-ray end time was generally found, but a significant fraction of events had also a different timing (Veronig et al. 2002b). Tests of the “theoretical Neupert effect”, i.e. comparisons of the beam power supply of hard X-ray-emitting electrons and the thermal energy of evaporated plasma observed in soft X-rays, was found strongly to depend on the lower nonthermal energy cutoff (Veronig et al. 2004). In this paper we systematically determine the plasma cooling times as function of energy, which would allow a more quantitative description of the Neupert effect.

In this paper we develop first a theoretical model of the spectral and temporal functions of a multi-temperature plasma that is cooled by thermal conduction (§2), then we describe the steps of our data analysis and model-fitting process applied to a specific flare (§3), then we carry out this analysis for a large statistical sample, describe some individual events, give statistical results (§4), and draw conclusions (§5).

2. THEORETICAL MODEL

In this Section we formulate the theoretical framework that quantifies the energy-dependent time delays that we can observe with RHESSI data in terms of a multi-temperature flare model where the cooling of the

flare plasma is governed by thermal conduction. This theoretical model is then fitted to RHESSI data in the following Sections.

2.1. Multi-Thermal Spectrum

The bremsstrahlung spectrum $F(\epsilon)$ of an isothermal plasma with temperature T , as a function of the photon energy $\epsilon = h\nu$, setting the coronal electron density equal to the ion density ($n = n_i = n_e$), and neglecting factors of order unity, such as from the Gaunt factor, $g(\nu, T)$, and the ion charge number, $Z \approx 1$, is (Brown 1974; Dulk & Dennis 1982),

$$F(\epsilon) \approx 8.1 \times 10^{-39} \int_V \frac{\exp(-\epsilon/k_B T)}{T^{1/2}} n^2 dV \quad (\text{keV s}^{-1} \text{ cm}^{-2} \text{ keV}^{-1}) . \quad (1)$$

Introducing the *total differential emission measure (DEM) distribution*, which specifies the squared electron density $n^2(T)$ at temperature T integrated over the total flare volume V ,

$$\frac{dEM(T)}{dT} = n^2(T) dV , \quad (2)$$

the hard X-ray spectrum of a multi-thermal flare plasma can be written as,

$$F(\epsilon) \approx 8.1 \times 10^{-39} \int \frac{\exp(-\epsilon/k_B T)}{T^{1/2}} \frac{dEM(T)}{dT} dT . \quad (3)$$

An example of such a multi-thermal hard X-ray spectrum is shown in Fig. 1 for a DEM that falls off as a powerlaw function of the temperature in the range of $T \geq 10$ MK, i.e., $dEM(T)/dT \propto T^{-\delta}$ with $\delta = 4.0$. The resulting photon spectrum can be approximated with a powerlaw function $F(\epsilon) \propto \epsilon^{-\gamma}$ with $\gamma = 4.6$ in the energy range of $\epsilon = 10 - 20$ keV, in which we focus our multi-thermal spectral analysis.

Simulating such multi-thermal spectra $F(\epsilon)$ (Eq. 3) for a range of DEM distribution functions with a powerlaw form,

$$\frac{dEM(T)}{dT} \propto T^{-\delta} , \quad (4)$$

say in a range of $\delta \approx 3 - 10$, we find the following empirical dependence of the photon (powerlaw) spectral index γ (evaluated in the energy range of $\epsilon = 10 - 20$ keV) (Fig. 2),

$$\gamma(\delta) \approx 3.60 + 0.062 \delta^2 . \quad (5)$$

2.2. Thermal Energy Ratio

We want to investigate by what temperature a given hard X-ray photon energy is dominated in a multi-thermal spectrum. For this purpose we define an energy ratio q_e that expresses the ratio of the observed photon energy ϵ in a hard X-ray spectrum to the thermal energy $\epsilon_{th} = k_B T$ of the temperature T that dominates the spectrum at the observed photon energy ϵ ,

$$\epsilon(T) = q_e \epsilon_{th} = q_e k_B T = q_e \epsilon_0 \left(\frac{T}{T_0} \right) , \quad T_0 = 11.6 \text{ MK} , \quad \epsilon_0 = 1 \text{ keV} . \quad (6)$$

From the simulated multi-thermal spectrum in Fig. 1 it can be seen that the energy factors q_e can numerically be determined at the intersections of two subsequent thermal spectral components. The ratio q_e depends

mostly on the DEM distribution function (which we quantified with a powerlaw index δ in Eq. 4), as well as slightly on the photon energy ϵ (or thermal energy ϵ_{th}). We simulate multi-thermal spectra (as shown in Fig. 1) and show the dependence of the energy ratio q_e on the thermal energy ϵ_{th} and DEM powerlaw index δ in Fig. 3 (top panel and bottom left), which can be approximated by,

$$q_e(\delta, T) \approx q_e(\delta) \left(\frac{T}{T_0}\right)^{0.03} \approx (0.52 + 0.95\delta) \left(\frac{T}{T_0}\right)^{0.03}. \quad (7)$$

Since the photon spectral index γ is a direct observable, it is more practical to express the energy factor as a function of γ , using the approximation $\gamma(\delta)$ given in Eq. 5,

$$q_e(\gamma) = \left[0.52 + 0.95 \sqrt{\frac{(\gamma - 3.60)}{0.062}} \right]. \quad (8)$$

This dependence $q_e(\gamma, T)$ is shown in Fig. 3, which approximately follows the proportionality $q_e \approx \gamma$ for $\gamma \gtrsim 4$. This gives a very simple rule of thumb to estimate what photon energy is dominated by a given temperature in a multi-thermal spectrum. For instance, if a multi-thermal photon spectrum has a spectral slope of $\gamma \approx 4$, then a temperature component of $T \approx 12$ MK (which corresponds to a thermal energy of $\epsilon_{th} = k_B T \approx 1.0$ keV) will dominate the spectrum at photon energies of $\epsilon = q_e \epsilon_{th} \approx \gamma \epsilon_{th} \approx 4.0$ keV. If the photon spectral index is $\gamma \approx 8$, the affected photon energy will be $\epsilon \approx 8$ keV.

A lower limit of the photon spectral index of a multi-thermal spectrum is $\gamma \geq 3.60$ (according to Eq. 8), for a DEM distribution that falls off with higher temperatures (i.e., $\delta \geq 0$).

If we express the the photon energy as function of the temperature, we thus have the scaling (with Eqs. 6-7),

$$\epsilon(T) = \epsilon_0 q_e(\gamma) \left(\frac{T}{T_0}\right)^{1.03}. \quad (9)$$

2.3. Temperature Scaling of Conductive Cooling

Flare plasma cooling at initially hot temperatures ($T \gtrsim 10$ MK) is dominated by conductive cooling, observable in soft X-rays, while the later phase of cooling visible in EUV ($T \lesssim 2$ MK) is dominated by radiative cooling (Antiochos & Sturrock 1978; Culhane et al. 1994; Aschwanden & Alexander 2001). For modeling of RHESSI data at energies $\epsilon \geq 1$ keV ($T \geq 11.6$ MK) we can therefore assume predominant conductive cooling. The conductive cooling time τ_c is given by the ratio of the thermal energy and the conductive loss rate,

$$\tau_c = \left(\frac{\epsilon_{th}}{dE/dt_{cond}}\right) = \left(\frac{3n_e k_B T}{\frac{d}{ds} \kappa T^{5/2} dT/ds}\right) = \left(\frac{3n_e k_B T}{\frac{2}{7} \kappa d^2 T^{7/2}/ds^2}\right) \approx \frac{21}{2} \frac{n_e L^2 k_B}{\kappa} T^{-5/2}. \quad (10)$$

If we want to express the dependence of the conductive cooling with flare temperature T , we have also to include the temperature scaling of the density $n_e(T)$, flare volume $V(T)$, and of the flare loop half length $L(T)$. Let us assume powerlaw scaling laws, with a power law index α_L for the loop length

$$L(T) \propto T^{-\alpha_L}, \quad (11)$$

and a power law index α_V for the flare volume,

$$V(T) \propto T^{-\alpha_V}. \quad (12)$$

Since we already defined a scaling law for the total emission measure as function of temperature in Eq. (4), we obtain for the electron density the following scaling law (using Eqs. 2, 4, 12),

$$n_e(T) \propto \left[\frac{T^{-\delta}}{V(T)} \right]^{(1/2)} \propto \left(\frac{T^{-\delta}}{T^{-\alpha_V}} \right)^{(1/2)} \propto T^{-(\delta-\alpha_V)/2}. \quad (13)$$

Combining these scaling laws we can now obtain the temperature scaling law of the conductive cooling time,

$$\tau_c(T) = \frac{21}{2} \frac{n_e(T) L^2(T) k_B}{\kappa} T^{-5/2} = \tau_{c0} \left(\frac{T}{T_0} \right)^{-\beta}, \quad (14)$$

with the powerlaw exponent

$$\beta = \frac{1}{2}[5 + \delta - \alpha], \quad \alpha = \alpha_V - 4\alpha_L. \quad (15)$$

and the constant

$$\tau_{c0} = \frac{21}{2} \frac{n_0 L_0^2 k_B}{\kappa T_0^{5/2}}, \quad T_0 = 11.6 \text{ MK}, \quad (16)$$

where all constants n_0 , L_0 refer to the temperature of $T_0 = 11.6 \text{ MK}$ ($\epsilon_{th} = 1 \text{ keV}$). Since we can determine the photon spectral index δ and the best-fit value of β , we can infer the value α from Eq. (15),

$$\alpha = 5 + \delta - 2\beta. \quad (17)$$

For a specialized flare model where a flare consists of heated loops all having the same length L at different temperatures, L_0 is then a constant, or $\alpha_L = 0$, and $\alpha = \alpha_V$.

2.4. Multi-Thermal Delays

If we observe thermal emission from photons with energy ϵ , the e-folding time over which these thermal photons radiate is approximately the conductive cooling time. For soft X-ray emission that peaks at time t_0 , e.g., parameterized with a symmetric time profile (e.g., a Gaussian function with width τ_g),

$$F(\epsilon, t) = F_0(\epsilon) \exp\left(-\frac{(t-t_0)^2}{2\tau_g^2}\right), \quad (18)$$

we can therefore characterize the time profile of cooling plasma by a convolution with the e-folding cooling time,

$$f(\epsilon, t) = \int_{-\infty}^t F(\epsilon, t') \exp\left(-\frac{(t-t')}{\tau_c}\right) dt' = F_0(\epsilon) \int_{-\infty}^t \exp\left(-\frac{(t'-t_0)^2}{2\tau_g^2}\right) \exp\left(-\frac{(t-t')}{\tau_c}\right) dt'. \quad (19)$$

This characterization essentially corresponds to the *Neupert effect* (Hudson 1991; Dennis & Zarro 1993) which states that the soft X-ray emission time profile corresponds to the time integral of the hard X-ray emission, which is the asymptotic limit for very long cooling times (i.e., $\tau_c \mapsto \infty$ in Eq. 19).

The convolution of a Gaussian time profile with an e-folding cooling time delays the peak of the emission, as a function of the Gaussian width τ_g and cooling time τ_c . Since the integral of Eq. 19 cannot be expressed in a closed analytical form, we determine the delay of the peak time by numerical simulations of Eq. 19. The numerically determined delays are plotted in Fig. 4, which can be approximated with the following simple analytical function,

$$\Delta t \approx \tau_g \frac{7}{4} \left[10 \log\left(1 + \frac{\tau_c}{\tau_g}\right) \right]^{3/4}. \quad (20)$$

We see that the delay Δt is proportional to the time scale τ_g of the unconvolved Gaussian function and scales with the ratio (τ_c/τ_g) , so the delay characteristics are invariant for time profiles that are normalized in duration. In the limit of relatively short cooling times ($\tau_c \ll \tau_g$), the delay vanishes as expected, while in the opposite limit ($\tau_c \gg \tau_g$), the delay increases nearly logarithmically.

Since we can measure time delays Δt as function of photon energies ϵ , we insert the temperature dependence on the photon energy ϵ (from Eq. 9),

$$\left(\frac{T}{T_0}\right) = \left(\frac{\epsilon}{q_e(\gamma)\epsilon_0}\right)^{0.97}, \quad (21)$$

and obtain the conductive cooling time (Eq. 10) as a function of photon energy ϵ ,

$$\tau_c(\epsilon) = \tau_{c0} \left(\frac{\epsilon}{q_e(\gamma)\epsilon_0}\right)^{-0.97\beta}. \quad (22)$$

This way we can express the cooling delay Δt (Eq. 20) as a function of the photon energy ϵ and photon spectral index γ (which are both observables),

$$\Delta t(\epsilon, \gamma) \approx \tau_g \frac{7}{4} \left[10 \log \left(1 + \frac{\tau_{c0}}{\tau_g} \left(\frac{\epsilon}{q_e(\gamma)\epsilon_0}\right)^{-0.97\beta} \right) \right]^{3/4}. \quad (23)$$

At higher energies, say above 30 keV, we expect that the nonthermal hard X-ray spectrum dominates over these thermal effects and that the relative delay is essentially zero (neglecting time-of-flight delays and trapping delays, which are generally significantly shorter than thermal delays). Therefore we define the relative delays with respect to a nonthermal energy value ϵ_{nth} ,

$$\Delta t_{th}(\epsilon) = \Delta t(\epsilon) - \Delta t(\epsilon_{nth}). \quad (24)$$

In Fig. 5 we show the expected delays $\Delta t_{th}(\epsilon)$ for durations of $\tau_g = 10$ s in the energy range of $\epsilon = 10 - 50$ keV, assuming a flare density $n_e = 10^{11} \text{ cm}^{-3}$, a flare loop half length of $L = 10^9 \text{ cm}$, the Spitzer conductivity $\kappa = 9.2 \times 10^{-7} \text{ erg s}^{-1} \text{ cm}^{-1} \text{ K}^{-7/2}$, the Boltzmann constant $k_B = 1.38 \times 10^{-16} \text{ erg K}^{-1}$, yielding a reference conduction time of $\tau_{c0} = 344 \text{ s}$ ($\approx 5.7 \text{ min}$) at a reference temperature of $T_0 = 11.6 \text{ MK}$ ($\epsilon_0 = 1 \text{ keV}$). The flare densities can be a factor of 5 lower or higher, and the flare loop lengths about a factor 2 shorter or longer, so we expect that the conductive cooling time can be a factor of $(n_e/n_0)(L/L_0)^2 = 20$ shorter or longer, i.e. $t_{c0} \approx 20 \text{ s} - 2 \text{ hours}$.

In practice, a time structure observed at some photon energy ϵ is always a mixture of thermal and nonthermal contributions, and thus the observed delay is also a mixture of the thermal delay and the near-zero delay of nonthermal photons. In a first approximation we estimate that the observed thermal delay is weighted by the ratio w_{th} of thermal to all (combined thermal and nonthermal) photons,

$$\Delta t_{obs}(\epsilon) \approx w_{th}(\epsilon)\Delta t_{th}(\epsilon) + w_{nth}(\epsilon)\Delta t_{nth}(\epsilon) \approx w_{th}(\epsilon)\Delta t_{th}(\epsilon), \quad (25)$$

where the energy-dependent weighting factor $w_{th}(\epsilon)$ is given by the flux ratio,

$$w_{th}(\epsilon) = \frac{F_{th}(\epsilon)}{F_{th}(\epsilon) + F_{nth}(\epsilon)} = \frac{F_{th}(\epsilon)}{F_{tot}(\epsilon)}, \quad (26)$$

and the nonthermal weighting factor $w_{nth}(\epsilon)$ in this normalization fulfils

$$w_{nth}(\epsilon) = [1 - w_{th}(\epsilon)] \quad (27)$$

3. DATA ANALYSIS METHOD

3.1. Flare Selection

The *Ramaty High Energy Spectroscopic Solar Imager (RHESSI)* flare catalog contained 18,887 events from the start of the mission (2002 Feb 12) until the time of our analysis (2006 Mar 31). In order to obtain a well-defined representative sample of flares we select all events that have (1) a minimum peak count rate of $C \geq 300$ cts s⁻¹, (2) a minimum energy extent above $\epsilon \geq 25$ keV, (3) a maximum duration of $t_f \leq 10$ min (600 s), and we discard events with special data conditions and problems (rear segment counts were decimated sometime during flare [DR=flag in flare catalog], spacecraft eclipse/night sometime during flare [ED], flare ended in spacecraft night [EE], flare started in spacecraft night [ES], flare ongoing at end of file [FE], in fast rate mode [FR], flare ongoing at start of file [FS], data gap during flare [GD], flare ended in data gap [GE], flare started in data gap [GS], spacecraft in high-latitude zone during flare [MR], non-solar events [NS], spacecraft in SAA sometimes during flare [SD], flare ended when spacecraft was in SAA [SE], or flare started when spacecraft was in SAA [SS]). However we left events in our selection when the front segment counts were decimated sometime during the flare [DF] or when a particle event was occurring in the background [PE], because this was often the case and would reduce our sample too much. Given these selection criteria, we ended up with a dataset of 89 events for our data analysis. The criteria (1) of a minimum count rate and (2) a minimum energy range eliminates mostly the weak events (approximately GOES C-class level) which have insufficient count statistics for the purpose of our analysis. The third criterium of (3) a maximum duration limit is chosen because short flares have a simpler temporal structure, and thus produce less confusion in our analysis, as well as the demodulation of time profiles for long flare durations would require excessive computing time.

The 89 selected events are typical mid-size flares, with flare durations in the range of $t_f = 76 - 592$ s (median of 408 s) and peak count rates of $C = 304 - 5616$ cts s⁻¹ (median of 592 cts s⁻¹). None of these flares is affected by pulse pile-up (generally at count rates of $< 10^4$ cts s⁻¹). In the analysis we also avoided time segments with a change of the decimation state or attenuator state, which would introduce discontinuities and biases in the cross-correlation of time profiles. All selected flares have detected flux at least up to the $\epsilon = 25 - 50$ keV energy range.

3.2. Demodulation of Time Profiles

In the first step of our analysis we demodulated the time profiles of the 89 flares with a time resolution of $\Delta t = 0.1$ s, because the original data contain the modulations from the 9 grids of the spinning (with a period of $P \approx 4.1$ s) RHESSI spacecraft, which is a *rotation modulation collimator (RMC)* Fourier imager type (Lin et al. 2002). We bin the energy range into 20 channels: 10 channels with 1 keV steps ($\epsilon = 10, 11, 12, \dots, 19$ keV), 5 channels with 2 keV steps ($\epsilon = 20, 22, 24, \dots, 28$ keV), and 5 channels with 5 keV steps ($\epsilon = 30, 35, 40, \dots, 50 - 55$ keV). The time demodulation is accomplished with the algorithm HSLDEMULATOR of the SSW software (written by G. Hurford), which yields demodulated fluxes in non-equidistant time bins, which we interpolate onto an equidistant time grid with a step of $\Delta t = 0.1$ s. The raw RHESSI light curves contain random but energy-independent data gaps in each detector (Smith et al. 2003), rapid modulation at subsecond timescales by the collimator, and 2 and 4 second periodic energy-independent modulation due to internal shadowing in the grids. In each independent 0.1 s interval, the demodulator removes all of the first two and part of the latter timing artifacts. The remaining timing artifacts are both energy-independent and smoothed by 10 second boxcar averaging and are short compared

to the typical observed time scales of $t_{FWHM} \approx 20 - 100$ s.

An example of such demodulated time profiles is shown for event # 5 (2002-Feb-26, 10:25:52 UT flare) in Fig. 6 (top left frame), where the time profiles are plotted with time bins of $\Delta t = 0.5$ s, and the smoothed curves (with a boxcar of $t_{smooth} = 10$ s) are overplotted in the time window of $t - t_0 = 20 - 90$ after flare start (at t_0). The enlarged time profiles are shown in Fig. 6 in the bottom left panel.

3.3. Spectral Modeling

Since our model is an exclusive (multi-)thermal model, we have first to separate the thermal emission from the nonthermal hard X-ray emission. As a rule of thumb, thermal emission mostly occurs at energies $\epsilon \lesssim 25$ keV, while nonthermal bremsstrahlung emission dominates at higher energies $\epsilon \gtrsim 25$ keV, as spectral modeling from HXRBS/SMM has shown (e.g., see reviews by Dennis 1988; Dennis & Schwartz 1989). Recent spectral modeling with RHESSI, which has a much higher spectral resolution, however, shows that nonthermal hard X-rays can be detected down to ≈ 7 keV (e.g., see review by Dennis 2006), so the dividing line between thermal and nonthermal emission covers a considerable part of our analyzed energy range of $\epsilon = 10 - 50$ keV. Our approach of separating the thermal component is based on fitting first a powerlaw function to the nonthermal spectrum in the energy range of $\epsilon \approx 30 - 50$ keV, which is believed to be entirely nonthermal, and then to subtract the extrapolated nonthermal spectrum from the total flux spectrum to obtain the purely (multi-)thermal spectrum at lower energies.

An example is shown in Fig. 6 (top right panel), where the total photon spectrum is shown in the energy range of $\epsilon = 10 - 50$ keV, integrated over the selected time interval, in units of photons $\text{s}^{-1} \text{cm}^{-2} \text{keV}^{-1}$, using the SSW software. Photon spectra can be obtained directly from the inversion of the count spectrum using only the diagonal elements of the instrument response matrix (so-called semi-calibrated spectra), when the following conditions hold: (1) only front segments are used; (2) the flare spectrum is at least 10 times the background spectrum for all energies; (3) the energy range is limited to $\epsilon \approx 10 - 50$ keV, which is all fulfilled in our analysis. Comparisons with spectral fits from the fully-calibrated and background-subtracted data using the OSPEX software were carried out in a few flares and we found almost identical results.

In the example shown in Fig. 6 we choose the energy range of $\epsilon = 30 - 50$ keV to fit a powerlaw function and obtain a powerlaw slope of $\gamma_{nth} = 2.0$ in this energy range. We extrapolate this nonthermal spectrum to lower energies (dotted line in Fig. 6 top right) to estimate the nonthermal contamination at lower thermal energies (ignoring a possible low-energy cutoff). Subtracting this extrapolated nonthermal spectrum from the total flux spectrum yields than an estimated pure (multi-thermal) spectrum (crosses in Fig. 6 top right), which can also be fitted by a powerlaw function, for which we obtain a powerlaw slope of $\gamma_{th} = 6.3$. This value can now be used to estimate the powerlaw index of the total differential emission measure distribution (Eq. 4), using the approximation given in Eq. (5), i.e., $\delta = \sqrt{(\gamma_{th} - 3.60)/0.062} = 6.6$. Thus the total DEM distribution falls off as $dEM(T)/dT \propto T^{-6.6}$ in the $\epsilon = 10 - 20$ keV range. Furthermore, the thermal powerlaw index δ allows us then to estimate the energy factor $q_e = \epsilon/\epsilon_{th} \approx 0.52 + 0.95 \delta = 6.8$ (Eq. 7) between photon energies ϵ and thermal energies ϵ_{th} . Therefore, the temperature range that dominates the $\epsilon = 10 - 20$ keV photons corresponds to $\epsilon_{th} = \epsilon/6.8 \approx 1.5 - 3.0$ keV, which is $T = \epsilon_{th}/k_B \approx 17 - 35$ MK.

The example in Fig. 6 shows also the cross-over of the (multi-)thermal and nonthermal spectrum at $\epsilon_{th} = 16.6$ keV, where both components are equally strong. The spectrum below this cross-over is dominated by thermal plasma, while the spectrum above is dominated by nonthermal emission. This is a new way to separate the thermal from the nonthermal component in a fairly accurate way. As long as the low-energy

cutoff of the nonthermal spectrum is somewhat below this cross-over energy, our powerlaw extrapolation of the nonthermal spectrum to lower energies renders a relatively accurate estimate of the purely (multi-)thermal spectrum.

3.4. Thermal Delay Measurement

We formulated our multi-thermal model based on thermal conductive cooling in terms of an energy-dependent delay $\Delta t(\epsilon, \gamma_{th})$, expressed as a function of the photon energy ϵ and the parameters τ_g , τ_{c0} , $q_e(\gamma_{th})$, and β (Eq. 23). We discussed already how we determined the energy ratio $q_e(\gamma_{th})$ based on the spectral modeling described above (§3.3). Next we can measure the FWHM directly from the time profile of the lowest nonthermal energy, which yields $t_{FWHM} = 27.5$ s for the example shown in Fig. 6 (bottom left), where we used for the lowest nonthermal energy $\epsilon_{nth} = 30$ keV. From the FWHM we can then calculate the Gaussian width $\tau_g = t_{FWHM} / (2\sqrt{2 \ln 2}) = t_{FWHM} / 2.35 = 11.7$ s. Therefore, the only two free parameters left are the reference conductive cooling time τ_{c0} and the powerlaw exponent β (Eq. 15) of the delay curve $\Delta t(\epsilon)$. We will determine these two free parameters from fitting our model $\Delta t(\epsilon)$ (Eq. 23) to observed delay measurements $\Delta t_{obs}(\epsilon_i)$, $i = 1, \dots, 20$.

We measure the relative delays between the time profiles of two adjacent energy channels by the standard cross-correlation function. In the example shown in Fig. 6 (bottom left) we can see that the highest energies ($\epsilon = 50$ keV) peak around $t - t_0 = 51$ s, while the lowest energies ($\epsilon \approx 10$ keV) peak around $t - t_0 = 67$ s, so there is a maximum delay of $\Delta t = 16$ s. We plot the relative delays in Fig. 6 bottom right and fit our theoretical model (thick line) by varying the free parameters. In fact, there is a third free parameter that contains the small time difference dt_{nth} between the time reference of nonthermal energies and the best-fit timing. In the example shown in Fig. 6 bottom right we find for the three free parameters a best fit at $t_{c0} = 301$ s, $dt_{nth} = 0.04$ s, and $\beta = 2.8$. Using the relation Eq. (17) we find for the volume powerlaw index $\alpha = 6.1$, so the volume of heated plasma falls off steeply with higher temperature.

In order to judge the goodness-of-fit, we want to calculate the χ^2 of the best fit. We repeat each cross-correlation between adjacent energy channels 100 times with added Poisson noise (according to the photon count statistics) and obtain a scatter in the relative delay measurements, which we define as standard deviation of each delay measurement $\Delta t_i \pm \sigma_{\Delta t, i}$. The reduced χ^2 is then computed in the standard way from the squared differences between the observed and theoretical delays summed over all energy channels. In the example shown in Fig. 6 (bottom right) we find a mean standard deviation in the uncertainties of delay measurements of $\sigma_{\Delta t, i} = 0.3$ s, and a goodness-of-fit of $\chi = \sqrt{\chi_{red}^2} = 1.1$, which is a fully acceptable fit. Note that the analytical model of the pure thermal delay according to Eq. (23) is shown as a thin solid line in Fig. 6 (bottom right), while the fitted delay (thick solid line in Fig. 6 bottom right) is based on the thermal weighting obtained from the spectral flux modeling (see ratio of thermal to total flux in spectrum shown in Fig. 6 top right).

3.5. Thermal Conduction Time Measurement

The main parameter we obtain from fitting the model to real data is the conduction cooling time scale τ_{c0} at the reference temperature $T_0 = 11.6$ MK (=1 keV). The conductive cooling time is proportional to

the product $n_0 L_0^2$ (Eq. 16), which can be written in dimensionless form as

$$\tau_{c0} = 344 \left(\frac{L_0}{10^9 \text{ cm}} \right) \left(\frac{n_0}{10^{11} \text{ cm}^{-3}} \right)^2 \quad [\text{s}]. \quad (28)$$

We measured a similar value of $\tau_{c0} = 301$ s in the example shown in Fig. 6. Thus we can constrain the product $L_0 n_0^2 \approx 10^{31} \text{ cm}^{-1}$, but we cannot determine the two parameters L_0 and n_0 independently.

The best-fit result predicts the conductive cooling time as function of temperature, which falls off as $\tau_c(T) = \tau_{c0}(T/T_0)^{-\beta}$ (Eq. 14). For the example shown in Fig. 6 we thus expect cooling times of $\tau_c(T = 17 \text{ MK}) = 301(17/11.6)^{-2.8} = 103$ s at $\epsilon = q_e \epsilon(T/T_0) = 6.8 * (17/11.6) = 10$ keV, which falls off to $\tau_c(T = 35 \text{ MK}) = 301(35/11.6)^{-2.8} = 14$ s at $\epsilon = q_e \epsilon(T/T_0) = 6.8 * (35/11.6) = 20$ keV. We test this prediction by convolving the nonthermal time profile with the corresponding e-folding cooling times and compare them with the observed time profiles in Fig. 7. The close agreement of observed and theoretically predicted time profiles corroborates the self-consistency of the data analysis method (in terms of energy-dependent time delay measurements) with the theoretical model (defined in terms of e-folding cooling times).

4. RESULTS

4.1. Fit Statistics

All 89 selected events have been fitted with the procedure described in Section 3. Table 1 reflects the results of the fit statistics. There are a number of cases that are not suitable for model fitting, such as events with too low count rate statistics, or events with complicated spectral evolution. Events with low count rates produce large uncertainties in the delay measurements, for which the repeated cross-correlation with added noise produces a large scatter. We find that events with a mean uncertainty in the time delay measurement $\Delta t \pm \sigma_{\Delta t}$ in excess of $\sigma_{\Delta t} \geq 2.0$ s are quite insensitive to the fitted model and produce also a too low χ^2 -value, so we consider these cases as unsuitable for model-fitting, which is the case for 21 out of the 89 selected events. Another category of unsuitable data are those with a too small energy range. In principle we try to fit all 20 energy channels (10-50 keV) with our model, but we have to eliminate those high-energy channels where the signal is not significantly above the noise level, and also those low-energy channels with no flux peak in the fitted time window (e.g., when a weak peak is superimposed on the flank of a steeply increasing longer time structure). We require a minimum of 10 energy channels to be usable for fitting, which eliminates another 3 events out of the 89 selected events. So, we are left with 65 events suitable for model fitting.

Out of the 65 fittable events (100%), we find that our model successfully fits the data in 44 cases (68%), having a goodness-of-fit of $\chi = \sqrt{\chi_{red}^2} \leq 2.0$, while the remainder of 21 events (32%) has unacceptable fits ($\chi \geq 2.0$) or unphysical solutions with e-folding (conduction cooling) times significantly larger than the flare duration ($t_{c0} > 2t_f$) or extremely short ($t_{c0} < 1.0$ s). A detailed investigation of the failures exhibits complex time structures, where subsequent time structures cannot be separated and have different spectral properties, yielding unphysical solutions when averaged. So, the failures do not necessarily mean that they are not consistent with the theoretical model, but merely that our fitting procedure that requires a single dominant time structure (or multiple structures with similar spectral characteristics) is not adequate in these cases. However, a more general fitting procedure that deals with the spectral evolution by convolving multiple time structures with variable spectra could save those cases.

4.2. Individual Cases

An exemplary subset of events (#5, 14, 30, 32, 34, 45, 60, 77 of our selection) is shown in Fig. 8, which contains the 8 most reliable fits (out of the 65 fittable cases): This subset has been selected by the criteria of small time delay uncertainties ($\sigma_{\Delta t} < 1.0$ s), a tight goodness-of-fit ($0.5 \leq \chi \leq 1.5$), a large fittable energy range (≥ 17 energy channels out of 20), at least 5 channels of thermal coverage ($\epsilon_{th} \geq 15$ keV), and physical solutions for the conduction cooling time ($1.0 \text{ s} < t_{c0} < 2t_f$). These 8 exemplary cases are shown in Fig. 8, where we display the expanded time profiles, the spectral fitting, and the energy-dependent time delays obtained from model fitting.

Let us have a closer look at these 8 examples, to which we refer by the identification number (#1,...,89), indicated after the observation time labels in Fig. 8 (left panels). Event #5, 14, 30, and 77 seem to consist of a single dominant time structure, while events #34, 45 and 60 consist at least of two comparably dominant time structures, and event #32 has about 5 noticeable structures. Since the time delay measurements are conducted by cross-correlation between adjacent energy channels, the time profile does not need to be similar over large energy ranges, as long there is at least one single dominant feature in each pair of adjacent energy channels. In event #34 we see even that at low (thermal) and high (nonthermal) energies are two different time structures dominant, but the step-wise cross-correlation from channel to channel retrieves the relative delay without jumping from the first to the second structure, as it would for cross-correlations over larger energy steps and would produce unphysical solutions for the conductive cooling time. Thus, our cross-correlation procedure seems to be able to retrieve correct time delays even for cases with multiple structures.

Inspecting the photon spectra we see that all 8 cases (shown in Fig. 8, middle panels) have a steeper slope in the (multi-)thermal domain than in the nonthermal domain (which is also the case for all other analyzed cases), also called “broken powerlaws with a break-up” (Dulk, Kiplinger, & Winglee 1992). The *spectral break-up* is actually a necessary condition for our analysis, if we assume that the nonthermal powerlaw spectrum can be extrapolated to lower energies, otherwise we would obtain a negative thermal flux spectrum. The (multi-)thermal spectra have powerlaw slopes of $\gamma_{th} = 5.9, \dots, 7.2$, while the flatter nonthermal spectra has a powerlaw slope of $\gamma_{nth} = 2.0, \dots, 5.8$ for the 8 cases shown in Fig. 8. Thus, the nonthermal slopes are fairly representative for all flares, for which a typical range of $\gamma_{nth} = 2 - 7$ is found with a median value of 4-5 (Datlowe et al. 1974; Kane 1973; Dennis 1985). The powerlaw slope of the nonthermal spectrum is determined from typically 3 to 6 energy channels, which has less accuracy in the case of 3 or 4 channels, but the error in the nonthermal slope γ_{nth} causes a smaller relative error in the subtracted thermal slope γ_{th} and affects the energy factor q_e only slightly. The energy factor is found to have a fairly stable value of $q_e = 6.4 - 7.7$ in these 8 cases, regardless of the variations of the nonthermal slope, so the accuracy of the nonthermal spectral slope γ_{nth} is not crucial.

The break-up feature allows us to define a discriminatory energy ϵ_{th} between the thermal and nonthermal spectral regime, which we define from the cross-over of the (multi-)thermal powerlaw spectrum and the nonthermal powerlaw spectrum. Note that the spectrum in the transition from the (multi-)thermal to the nonthermal portion curves continuously from the steep thermal slope to the flat nonthermal slope, which is a predicted feature of our model. The cross-over energy demarcates the energy where the thermal and nonthermal spectrum has equal flux and is found in an energy range of $\epsilon_{th} = 16.7, \dots, 26.7$ keV for the 8 cases shown in Fig. 8. The spectrum at energies below this cross-over is dominated by thermal electrons, while nonthermal electrons dominate above it.

The cross-over between thermal and nonthermal is typically at $\epsilon_{th} = 15 - 20$ keV. We find only two exceptions where the cross-over occurs at significantly different energies (see column ϵ_{th} in Table 2). There

are the two events #21 and 83, where the cross-over occurs as low as $\gtrsim 10 - 11$ keV (Fig. 10). Note that in both flares there is a very short impulsive heating pulse ($t_g \approx 6 - 8$ s) that extends up to $\epsilon \approx 40$ keV. The thermal contamination and the associated delays are measurable in the energy range of $\epsilon \approx 10 - 20$ keV, but is not dominant across the entire spectrum above 10 keV.

The energy-dependent time delay fits are shown in Fig. 8 (right panels) and Fig. 9 for all fittable 44 cases. The time delays show the thermal vs. nonthermal characteristics in the time domain. In the thermal domain the delay increases systematically with lower energies, while the nonthermal domain shows no delay. The spectrally determined cross-over energy ϵ_{th} is also marked in time delay panels (Fig. 8 right and in Fig. 9), which closely coincides with the separatrix between thermal and (near-zero) nonthermal delay characteristics, and thus corroborates the consistency between the two methods applied in the spectral and time domain.

The time delay panels shown in Fig. 8 (right panels) and Fig. 9 reveal also a number of other interesting characteristics. The maximum delays measured at 10 keV can be very large, up to $\Delta t = 20 - 30$ s (cases #32, 34, 39, 65, 66, 79, 84), while the uncertainties of the delays is always much shorter $\sigma_{\Delta t} \leq 2.0$ s, so these cases are most sensitive to the model fits. Other cases have relatively short delays of $\Delta t \leq 5.0$ s (cases #26, 37, 48, 61, 71, 72, 76, 83, 85, 86), only a few times larger than the uncertainties of the time delays, and thus are less sensitive to the detailed functional shape of the model. Another criterion that determines the sensitivity to the model is the energy extent of the thermal part. The model is well-constrained if there are at least 10 energy channels in the thermal domain, i.e., events with starting energies of $\epsilon_{min} = 10$ keV and cross-over energies of $\epsilon_{th} \geq 20$ keV, which is the case for the events # 14, 30, 32, 34, 37, 39, 40, 41, 59, 60, 61, 66, 77, 79, 81, 84, and 86. On the other hand, in a few cases we notice that the nonthermal delays are not consistent with a predicted near-zero delay, which cannot be explained by our conduction-cooling model. These few cases show a time delay that increases with energy, as expected for collisional trapping (Aschwanden et al. 1997). Those cases need to be modeled with a combined thermal conduction plus trapping model (to be presented in a follow-up paper). In our thermal model fit these cases drop out because they exhibit an unacceptable large χ^2 -value ($\chi \gg 1.0$).

4.3. Discussion of Parameter Statistics

The flare observing times and inferred physical parameters are listed in Table 2 for all 44 events with acceptable fits ($\chi \leq 2.0$), and the averages and standard deviations are listed in Table 3.

The time scales we analyzed in these flares include the FWHM durations of the cross-correlated time profile segments found to be useful for measuring thermal delays. This FWHM duration, which has a mean of $t_{FWHM} = 55 \pm 46$ s is about a factor 7 shorter than the mean flare duration $t_f = 398 \pm 115$ s. So, a flare typically contains multiple episodes where the flux varies by more than 50%, probably originating from different spatial locations. We found that the thermal delays could be most reliably measured in time segments that bracket a flux peak below 50% of its peak value (yielding a well-defined FWHM), otherwise the cross-correlation is subject to a “profile-asymmetry bias”. Such flux peaks, however, can contain multiple subpeaks (or nonthermal electron injection pulses), as shown in events #32, 34, 45, 60 in Fig. 8. So, the peaks with a duration of $t_{FWHM} \approx 1$ min selected here do not represent “elementary flare bursts” (with durations of $t_{FWHM} \approx 4 - 24$ s characterized by De Jager & De Jonge (1978).

Regarding spectral properties we characterized the nonthermal spectrum (in the $\epsilon \approx 30 - 50$ keV range) with a powerlaw function and found a mean slope of $\gamma_{nth} = 3.5 \pm 1.1$, which seems to be a representative value

for all flares (Datlowe et al. 1974; Kane 1973; Dennis 1985), so the selected flare events are not particularly soft or hard, or part of a special flare category, such as classified by Tanaka (1983), who specified a special class of thermal flares with temperatures of $T \approx 30 - 50$ MK. We found in all 89 analyzed flare a thermal component, with a cross-over at $\epsilon_{th} = 18.0 \pm 3.4$ keV, which corresponds (according to the measured ratio $q_e = 7.4 \pm 1.0$ of photon energies to thermal energies) to thermal energies of $\epsilon_{th} = 2.4 \pm 0.6$ keV, or temperatures of $T = 27.8 \pm 7.0$ keV, and thus overlaps with the low end of Tanaka’s category of *thermal flares*.

Although the thermal component of a flare generally can be fitted with a single temperature, we could fit the energy range of $\epsilon \approx 10 - 20$ keV with a multi-thermal model, approximated by a powerlaw function. This multi-thermal spectrum was found to have a mean slope of $\gamma_{th} = 6.9 \pm 0.9$, which is a fairly narrow range of values, almost a constant ($\gamma_{th} \approx 7$), while the nonthermal spectrum is flatter and has a relatively larger variation ($\gamma_{nth} = 3.5 \pm 1.1$). The almost constant slope of the multi-thermal spectrum implies also an almost constant ratio of photon to thermal energies, i.e., $q_e = 7.4 \pm 1.0$, or an almost constant fall-off of the DEM at the high-temperature side, i.e., $dEM(T)/dT \approx T^{-\delta}$ with a slope of $\delta = 7.2 \pm 1.0$. From the spectral slope δ and the best-fit value of β we were able to determine the volume scaling index $\alpha(\delta, \beta)$ (Eq. 17), which implies that the high-temperature plasma volume falls off with $V(T) \approx T^{-\alpha_V}$ and $\alpha_V \approx \alpha = 6.8 \pm 2.7$. This means that the volume of heated plasma decreases by about two orders of magnitude for every factor 2 in temperature (i.e., $2^{6.8} \approx 10^2$). Interestingly, this implies that the electron density is almost invariant as function of temperature, since $n_e(T) \propto T^{-(\delta-\alpha_V)/2}$ (Eq. 13) and $\delta \approx \alpha_V \approx \alpha$ according to our finding. This is in contrast to the scaling law between different flares, which generally behaves as $n_e(T) \propto T^2$ (Aschwanden 1999) if one combines flare observations over a large temperature range, from nanoflares (Aschwanden & Parnell 1997) to soft X-ray brightenings (Kano & Tsuneta 1995; Shimizu 1997) and large flares (Pallavicini et al. 1978; Aschwanden & Benz 1997). Our finding of $n_e(T) \approx const$ applies to the plasma distribution in single flares, which could be explained by a decreasing filling factor with higher temperature.

5. CONCLUSIONS

We analyzed the energy-dependent time delays of hard X-ray emission in the energy range of $\epsilon = 10 - 50$ keV with high-resolution spectra ($\Delta\epsilon = 1$ keV) from RHESSI in a representative set of 89 flares observed during 2002-2005. We found that the thermal and nonthermal domain of hard X-ray data does not only show a different characteristics in the spectral domain, but exhibits also a consistently different characteristics of the energy-dependent time delays between the two regimes. From the spectral analysis we found a discrimination borderline between the thermal and nonthermal domain from the cross-over of the two separated spectral components, which has a relatively narrow range of values with $\epsilon_{th} = 18.0 \pm 3.4$ keV. The energy-dependent time delays above this cross-over energy are found to be nearly zero in the nonthermal domain, while they increase with lower energy in the thermal domain, consistent with the convolution ($\tau_e(\epsilon) \propto \epsilon^{-\beta}$) with an e-folding time scale τ_e and powerlaw index $\beta = 2.7 \pm 1.2$.

On theoretical grounds it has been established earlier that the cooling of high-temperature ($T \gtrsim 10$ MK) plasma is dominated by thermal conduction, which scales with a similar scaling law ($\tau_c \propto T^{-5/2}$) and index ($\beta_{theo} = 2.5$) as we inferred from the observations ($\beta_{obs} = 2.7 \pm 1.2$). To be more accurate, the theoretical expression for the thermal conduction time includes also the electron density n_e and the flare loop length L , which might also have a temperature dependence and could modify the expected temperature dependence of the thermal conduction time. However, our observations imply that there is no significant temperature dependence in the product $n_e L^2$, either because they cancel out or none of the parameters n_e and L have

any significant temperature dependence. This result makes it easier to predict the temperature or energy dependence of the conductive cooling time without knowledge of the generally unknown electron density and flare loop length.

Our detailed analysis shows that the observed energy-dependent time delay systematically increases with lower energy. This continuous increase is the result of two effects: first of the increasing weighting of thermal to nonthermal emission with lower energy, and second the $T^{-5/2}$ dependence of the thermal conductive cooling time. If a flare would have only a single-temperature plasma, the predicted delay due to the conductive cooling time would be constant in the thermally dominant spectral regime, which is clearly not the case (see Appendix A). Therefore, the continuous increase of the delay with lower energy in the thermal domain convincingly indicates a multi-thermal plasma. In this study we have quantified this multi-thermal plasma with the total emission measure distribution $dEM(T)/T$, which was found to drop off at the high-temperature side with an approximate powerlaw of $\propto T^{-\delta}$ with $\delta = 7.2 \pm 1.0$. This evidence for multi-thermal plasma in virtually all flares suggests that hard X-ray spectra in the energy range of $\gtrsim 10$ keV should generally be fitted with a *multi-thermal spectrum*, rather than with a *single-temperature fit* as it was usually carried out in earlier studies. Our more accurate modeling of the multi-thermal spectrum yields also a better separation between the thermal and nonthermal domain, for which no reliable method was known before. The upshot is that the information in the time domain, i.e., energy-dependent time delay measurements, yields invaluable information about thermal, multi-thermal, and nonthermal spectral components that cannot be retrieved from spectral fitting alone.

All in all, this work is the first quantitative work on thermal delays in solar flares, conducted on a large representative sample of solar flares, using high-resolution spectra from RHESSI. This approach of quantitative modeling could in principle be done before the advent of high-resolution spectra from RHESSI, but the much poorer energy resolution of previous hard X-ray detectors (e.g., HXRBS/SMM, HXT/Yohkoh, BATSE/CGRO) would probably lead to only limited success in model-fitting. This study has shown that we can obtain fairly accurate prime physical parameters from combined spectral-temporal model-fitting with high-resolution spectra. The results convey overwhelming evidence that flares always contain multi-thermal plasma and that the flare plasma cooling is always dominated by thermal conduction at $T \gtrsim 10$ MK. Future studies may use the model developed here to extract the uncontaminated nonthermal electron injection profile in the time domain and the low-energy cutoff of the nonthermal spectral component, as well as quantify the detailed thermal and nonthermal energy budget in solar flares.

Acknowledgements: The author is grateful to Brian Dennis for helpful critical comments and to Gordon Hurford for providing the RHESSI demodulation algorithm. Support for this work was provided by the NASA contract NAS5-98033 of the RHESSI mission through University of California, Berkeley (subcontract SA2241-26308PG).

Appendix A: The Isothermal Model

Hard X-ray spectra have often been fitted with a single-temperature (isothermal) component in the thermal energy range plus a powerlaw component (or multiple powerlaws) in the nonthermal energy range, obtaining an acceptable goodness-of-fit (e.g., Lin et al. 1981; Benka & Holman 1994). However, in the late phase of flares, sometimes a superhot component with a temperature of $T \approx 35$ MK was found, besides the main flare plasma temperature of $T \approx 15$ MK, which had to be considered in fitting the hard X-ray spectrum (e.g., Lin et al. 1981). Also from analysis of cooling times in different energy or temperature

bands it is clear that the DEM distribution of flare temperatures has often a peak at a temperature of $T \approx 10 - 15$ MK, but the distribution of flare plasma temperatures tails off gradually from $T \gtrsim 15$ MK to $T \lesssim 40$ MK (Antiochos & Sturrock 1978; Culhane et al. 1994; Aschwanden & Alexander 2001). Therefore, our multi-thermal DEM model with a gradual fall-off at high temperatures is fully consistent with all these observations. Nevertheless, since hard X-ray spectra often have been fitted satisfactorily with a single temperature (which probably corresponds to the peak temperature of the DEM or the emission measure-weighted temperature), the question arises whether a single-temperature (or isothermal) model could also fit the observed energy-dependent time delays measured here.

We show the theoretical expectations for the two (multi-thermal and isothermal) models in Fig. 5. Essentially, the thermal delay is constant in the thermally dominant part of the spectrum for the isothermal model (because a single temperature produces a fixed conductive cooling time), while the thermal delay increases gradually towards lower energies in the multi-thermal model due to the $T^{-5/2}$ -dependence of the conductive cooling time. Since this effect might be confused with a second effect, the relative weighting between thermal and nonthermal (near-zero) delay, which also leads to a gradual increase of the observed delay in the intermediate (thermal/nonthermal) part of the spectrum, we perform some real fits of both models to demonstrate the difference in the goodness-of-fit. One case is shown in Fig. 11, where the multi-thermal fit is acceptable ($\chi = 1.0$, Fig. 11, left), while the isothermal fit is clearly unacceptable ($\chi = 6.0$, Fig. 11 right). The absolute time of the delay in the fits shown in Fig. 11 is controlled by the best-fit solution, which yields a slight offset of $\Delta t_{nth} = 0.83$ s in the multi-thermal model (Fig. 11, left), and a large negative delay $\Delta t_{nth} = -4.46$ s for the isothermal model (Fig. 11, right). This offset has not physical meaning, because the absolute reference time is a free parameter in our fitting method. So, this example clearly demonstrates what we expect from the theoretical models illustrated in Fig. 5. We performed the isothermal fits for the same 8 cases shown in Fig. 8 and list the goodness-of-fit in Table 4. The goodness-of-fit is acceptable for all multi-thermal fits ($\chi = 0.8 - 1.4$), while it is not acceptable for all isothermal fits ($\chi = 2.0 - 9.3$). These 8 examples clearly demonstrate that a single-temperature cannot fit the data, while our multi-thermal model is fully consistent with the data.

REFERENCES

- Antiochos, S. K., & Sturrock, P. A. 1978, ApJ, 220, 1137
- Aschwanden, M. J. & Alexander, D. 2001, Solar Physics, 204, 93
- Aschwanden, M. J., 2004, *Physics of the Solar Corona - An Introduction*, Praxis Publishing Ltd., Chichester UK, and Springer, Berlin, ISBN 3-540-22321-5
- Aschwanden, M. J., Schwartz, R. A., & Alt, D. M. 1995, ApJ 447, 923
- Aschwanden, M. J., Kosugi, T., Hudson, H. S., Wills, M. J., & Schwartz, R.A. 1996, ApJ 470, 1198
- Aschwanden, M. J., Bynum, R. M., Kosugi, T., Hudson, H. S., & Schwartz, R. A. 1997, ApJ 487, 936
- Aschwanden, M. J. & Benz, A. O. 1997, ApJ 480, 825
- Aschwanden, M. J. 1999, Solar Phys. 190, 233
- Aschwanden, M. J. & Parnell, C.E. 2002, ApJ 572, 1048
- Battaglia, M., Grigis, P., C., & Benz, A. O. 2005, A&A, 439, 737
- Benka, S. G. & Holman, G. D. 1994, ApJ 435, 469
- Cargill, P. J., Mariska, J. T., & Antiochos, S. K. 1995, ApJ 439, 1034
- Culhane, J. L., Phillips, A. T., Inda-Koide, M., Kosugi, T., Fludra, A., Kurokawa, H., Makishima, K., Pike, C. D., Sakao, T., Sakurai, T., Doschek, G. A., Bentley, R. D. 1994, Solar Phys. 153, 307
- Datlowe, D. W., Elcan, M. J., & Hudson, H. S. 1974, Solar Phys. 39, 155
- De Jager, C. & De Jonge G. 1978, Solar Phys. 58, 127
- Dennis, B. R. 1985, Solar Phys. 100, 465
- Dennis, B. R. 1988, Solar Phys. 118, 49
- Dennis, B. R. and Schwartz, R. A. 1989, Solar Phys. 121, 75
- Dennis, B. R. & Zarro, D. M. 1993, Solar Physics, 146, 177
- Dennis, B. R., Hudson, H. S., & Krucker, S. 2006, Proc. CESRA Workshop 2004, "The High Energy Solar Corona: Waves, Eruptions, Particles", Isle of Skye, Scotland
- Dulk, G. A. & Dennis, B. R. 1982, ApJ 260, 875
- Dulk, G. A., Kiplinger, A. L., & Winglee, R. M. 1992, ApJ 389, 756
- Fisher, G. H. & Hawley, S. L. 1990, ApJ 357, 243
- Hudson, H. S. 1991, Bull. Am. Astron. Soc., 23, 1064
- Kane, S. R. 1973, in *High Energy Phenomena of the Sun*, (eds. R. Ramaty & Stone, R. G.), NASA SP-342, 55
- Kano, R. & Tsuneta S., 1995, ApJ 454, 934
- Lin, R. P., Schwartz, R. A., Pelling, R. M., & Hurley, K. C. 1981, ApJ 251, L109

- Lin,R.P., Dennis,B.R., Hurford,G.J., Smith,D.M., Zehnder,A., Harvey,P.R., & 60 co-authors 2002, Solar Phys. 210, 3
- Pallavicini, R., Serio, S., & Vaiana, G.S. 1978, ApJ 216, 108
- Shimizu, T. 1997, PhD Thesis, Natl. Astron. Observatory, Mitka, Tokyo 181, Japan
- Smith,D.M., Lin,R.P., Turin,P., Curtis,D.W., Primbsch,J.H., Campbell,R.D., Abiad,R., Schroeder,P., and 12 co-authors 2002, Solar Phys. 210, 33
- Veronig, A., Temmer, M., Hanslmeier, A., Otruba, W., & Messerotti, M. 2002a, A&A, 382, 1070
- Veronig, A., Vrsnak, B., Dennis, B. R., Temmer, M., Hanslmeier, A., & Magdalenic, J. 2002b, A&A, 392, 699
- Veronig, A., Vrsnak, B., Temmer, M., & Hanslmeier, A. 2002c, Solar Phys., 208, 297
- Veronig, A., Brown, J. C., Dennis, B. R., Schwartz, R. A., Sui, L. S., & Tolbert, K. 2004, ApJ, 621, 482
- Vilmer, N., Kane, S. R., & Trotter, G. 1982, A&A 108, 306

Table 1. Event Statistics

Criteria	Number	
Number of cases	89	
Number of noisy cases ($\sigma_{\Delta t} > 2.0$ s)	21	
Number of insufficient energy coverage (< 10 channels)	3	
Number of fittable cases ($\sigma_{\Delta t} < 2$ s and > 10 channels)	65	100%
Number of not-acceptable fits ($\chi > 2$ or $t_{c0} < 1$ s or $t_{c0} > 2 * t_f$)	21	32%
Number of acceptable fits ($\chi < 2$ and $1 \text{ s} < t_{c0} < 2 * t_f$)	44	68%

Table 2. Parameters of flare events with acceptable model fits

#	Date	Start t_0 (UT)	Duration t_f (s)	Width t_g (s)	Index γ_{nth}	Index γ_{th}	Energy ϵ_{th} (keV)	Time t_{c0} (s)	Index β	Error $\langle \sigma_{\Delta t} \rangle$ (s)	Goodness χ
1	20-Feb-2002	11:04:20	468	9.1	2.2	5.4	18.2	76	3.3	0.7	0.5
3	23-Feb-2002	22:47:48	472	7.9	3.0	6.3	19.9	256	4.9	0.8	0.7
4	24-Feb-2002	23:14:36	448	27.7	3.1	7.3	13.4	33	2.8	1.1	1.1
5	26-Feb-2002	10:25:52	344	11.7	2.0	6.3	16.7	301	2.8	0.3	1.1
6	17-Mar-2002	10:11:36	552	10.2	2.7	7.3	18.0	152	3.9	0.8	0.6
10	9-Apr-2002	12:56:52	360	34.0	4.0	8.8	14.0	11	3.5	2.0	0.6
11	12-Apr-2002	13:07:36	512	14.9	3.4	6.3	21.4	52	3.2	0.9	0.7
12	14-Apr-2002	04:49:04	428	29.4	4.1	7.3	17.7	64	1.0	1.4	1.3
14	4-May-2002	02:46:48	364	10.6	2.3	6.3	24.5	246	3.8	0.9	1.0
17	29-May-2002	15:01:40	388	29.8	5.0	7.1	16.1	30	2.9	1.9	1.0
18	29-May-2002	15:48:28	536	7.2	3.5	7.1	14.7	90	3.7	0.5	0.7
21	29-Jun-2002	09:29:12	380	7.9	2.1	4.8	10.2	12	0.9	0.5	0.9
22	2-Jul-2002	22:35:40	408	12.8	3.3	7.6	16.1	4	0.7	1.7	0.6
23	2-Jul-2002	22:50:12	468	17.9	4.7	7.3	16.0	35	2.9	1.3	0.7
25	11-Jul-2002	14:16:48	360	21.7	4.2	8.1	18.3	79	2.6	1.4	1.2
26	14-Jul-2002	16:11:20	172	5.7	2.9	6.4	14.7	6	1.5	0.3	0.9
30	16-Aug-2002	22:08:24	512	8.9	4.0	5.9	27.7	103	3.6	0.4	1.0
32	18-Aug-2002	20:19:20	480	90.0	3.0	6.9	20.8	74	3.2	1.0	1.0
33	20-Aug-2002	22:42:08	372	10.6	3.1	7.5	17.4	10	1.3	0.7	0.6
34	21-Aug-2002	19:04:16	432	17.0	4.5	6.5	20.3	196	3.3	0.5	1.2
37	27-Aug-2002	12:28:00	204	23.4	5.4	7.6	19.2	4	3.2	1.7	0.9
39	31-Aug-2002	14:19:04	436	34.0	3.7	7.0	19.3	43	1.9	1.0	1.0
40	1-Sep-2002	09:30:56	484	21.3	4.3	7.5	19.1	5	1.0	1.0	0.8
41	5-Sep-2002	20:41:48	500	55.3	3.2	8.1	19.0	22	2.1	1.6	1.2
42	6-Sep-2002	16:23:56	400	20.2	4.3	7.9	16.2	44	3.6	0.9	0.9
45	30-Oct-2002	17:16:40	184	19.8	4.1	7.1	16.7	33	1.3	0.7	1.4
48	28-Nov-2002	04:35:40	124	8.5	2.2	5.7	13.7	38	4.8	1.1	0.5
49	9-Dec-2002	21:35:12	176	12.6	3.0	7.3	18.5	109	4.7	1.8	1.0
59	29-Jul-2003	01:34:04	540	34.0	4.1	7.9	19.2	13	2.2	1.4	0.9
60	5-Aug-2003	12:44:36	424	32.1	5.8	7.2	19.1	19	3.1	0.8	1.2
61	24-Sep-2003	12:52:00	336	12.8	1.9	6.3	19.4	7	4.5	1.8	1.0
65	16-Nov-2003	18:10:32	496	29.1	3.5	7.4	17.0	59	2.7	1.6	0.9
66	18-Nov-2003	01:34:52	540	49.4	5.5	7.8	18.5	35	2.1	1.2	1.1
71	18-Jan-2004	00:12:48	448	14.5	3.4	6.1	17.0	113	3.2	0.6	0.5
72	28-Feb-2004	03:23:12	180	12.3	1.8	6.5	17.1	2	1.5	1.0	0.7
76	18-Jul-2004	11:43:44	592	6.0	2.0	5.1	16.1	124	3.1	0.3	1.0
77	18-Jul-2004	14:11:40	400	19.1	2.4	6.8	24.0	27	2.1	0.7	0.8
79	13-Aug-2004	15:11:56	404	85.1	4.5	7.6	19.9	43	1.2	1.7	1.2
81	23-Oct-2004	19:19:16	372	21.3	3.2	7.9	19.7	19	1.0	1.8	1.5
83	5-Nov-2004	10:14:56	320	6.2	5.2	6.4	10.8	157	4.2	0.5	0.7
84	21-Jan-2005	10:12:56	504	13.6	3.2	7.1	19.3	745	3.4	0.4	1.9
85	30-Apr-2005	02:53:28	272	12.8	2.4	5.9	13.5	13	2.7	0.9	0.8
86	27-Jun-2005	08:46:04	312	51.1	4.4	5.3	22.8	17	2.0	0.9	1.8
87	9-Sep-2005	17:39:28	424	59.6	5.5	6.7	22.8	25	1.8	1.5	1.0

Table 3. Parameter Statistics

Parameter	Range	Average and standard deviation
Number of events in subset with acceptable fits	N=44	
Flare duration	$t_f = 124 - 592$ s	$t_f = 398 \pm 115$
FWHM of peak	$t_{FWHM} = 13 - 212$ s	$t_{FWHM} = 55 \pm 46$ s
Gaussian width of peak	$t_g = 6 - 90$ s	$t_g = 24 \pm 20$ s
Powerlaw index of nonthermal spectrum	$\gamma_{nth} = 1.8 - 5.8$	$\gamma_{nth} = 3.5 \pm 1.1$
Powerlaw index of thermal spectrum	$\gamma_{th} = 4.8 - 8.8$	$\gamma_{th} = 6.9 \pm 0.9$
Powerlaw index of DEM	$\delta = 4.4 - 9.2$	$\delta = 7.2 \pm 1.0$
Ratio of photon/thermal energy	$q_e = 4.8 - 9.2$	$q_e = 7.4 \pm 1.0$
Thermal/nonthermal cross-over energy	$\epsilon_{th} = 10 - 28$ keV	$\epsilon_{th} = 18.0 \pm 3.4$ keV
Thermal conduction cooling time	$\tau_{c0} = 2 - 745$ s	$\tau_{c0} = 10^{1.6 \pm 0.6}$ s
Powerlaw index of delay time	$\beta = 0.7 - 5.2$	$\beta = 2.7 \pm 1.2$
Powerlaw index of volume scaling	$\alpha = 1.3 - 11.7$	$\alpha = 6.8 \pm 2.7$
Uncertainty of time delay measurements	$\sigma_{\Delta t} = 0.3 - 2.0$ s	$\sigma_{\Delta t} = 1.0 \pm 0.5$ s
Goodness-of-fit	$\chi = 0.5 - 1.9$	$\chi = 0.96 \pm 0.31$

Table 4. Multi-thermal vs. Isothermal Fits

Flare #	Multi-thermal model	Isothermal model
	χ	χ
#5	1.1	3.8
#14	1.0	4.6
#30	1.0	6.0
#32	1.0	9.3
#34	1.2	7.6
#45	1.4	2.0
#60	1.2	5.4
#77	0.8	4.2

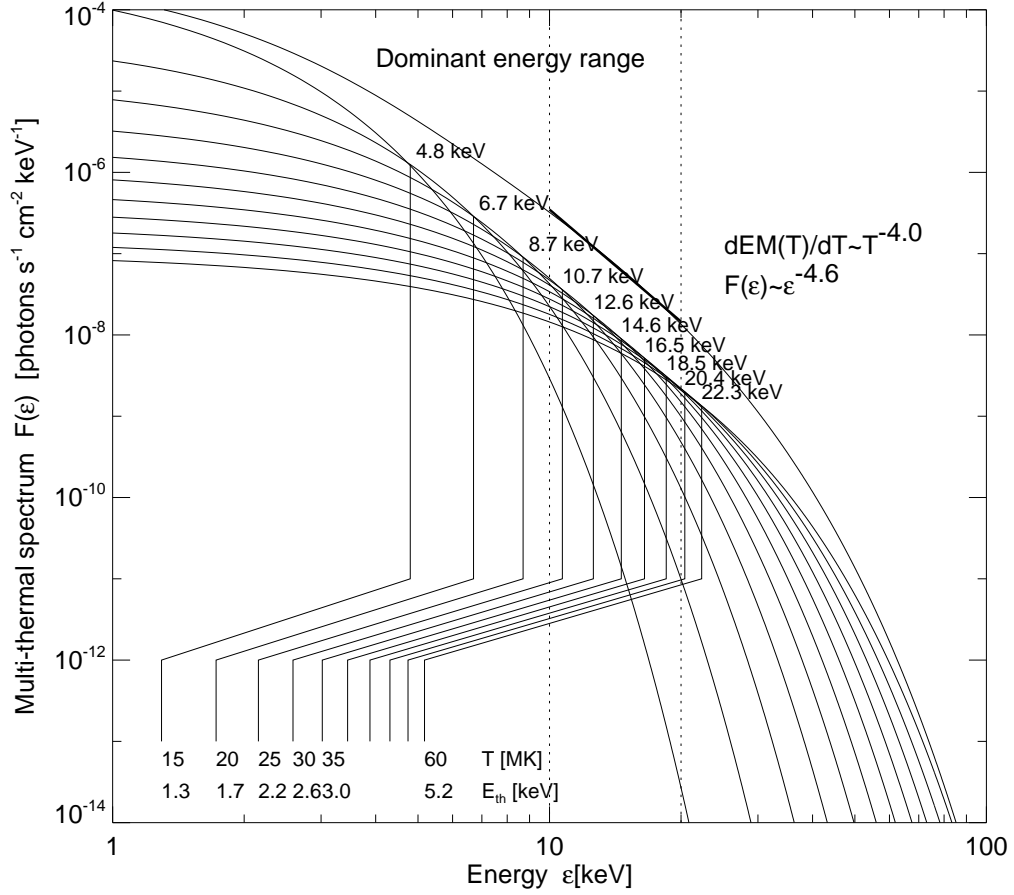


Fig. 1.— Example of a multi-thermal spectrum with contributions from plasmas with temperatures of $T = 15, 20, \dots, 60$ MK and a DEM distribution of $dEM(T)/dT \approx T^{-4}$. The individual thermal spectra and their sum are shown with thin linestyle, where the sum represents the observed spectrum. Note that the photons in the energy range of 4.8–22.3 keV are dominated by temperatures of $T=15$ –60 MK, which have a corresponding thermal energy that is about a factor of 4 lower (1.3–5.2 keV). The photon spectrum in the range of $\epsilon = 10 - 20$ keV is fitted with a powerlaw function (thick line), which has a slope of $F(\epsilon) \propto \epsilon^{-4.6}$.

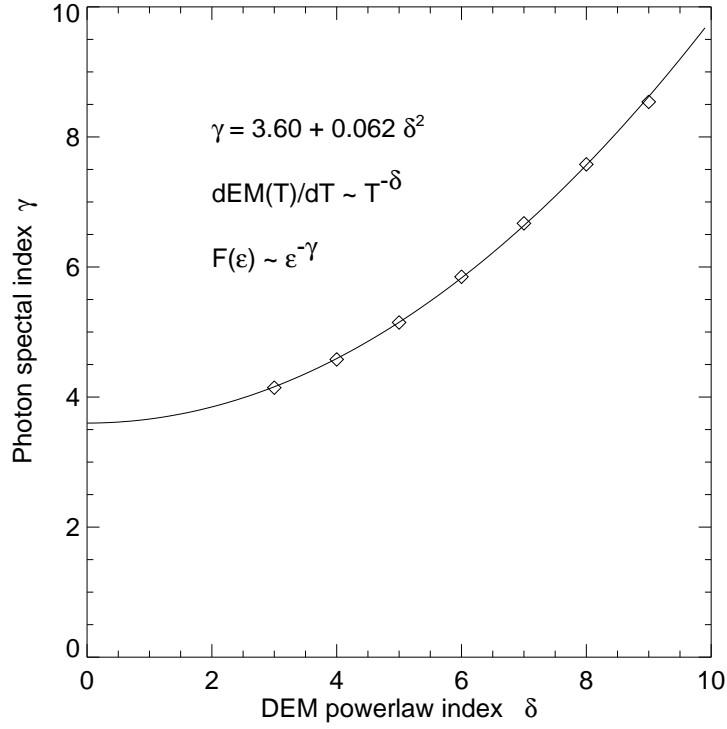


Fig. 2.— The multi-thermal photon spectrum (e.g., Fig. 1) is approximated with a powerlaw function $F(\epsilon) \propto \epsilon^{-\gamma}$ with powerlaw index γ in the energy range of $\epsilon = 10\text{--}20$ keV. The dependence of the powerlaw index $\gamma(\delta)$ is shown here as a function of the powerlaw index δ of the DEM distribution function $dEM(T)/dT \propto T^{-\delta}$. The simulated datapoints are marked with diamonds, and the fitted analytical approximation $\gamma(\delta) = 3.60 + 0.062 \delta^2$ is shown as a curve.

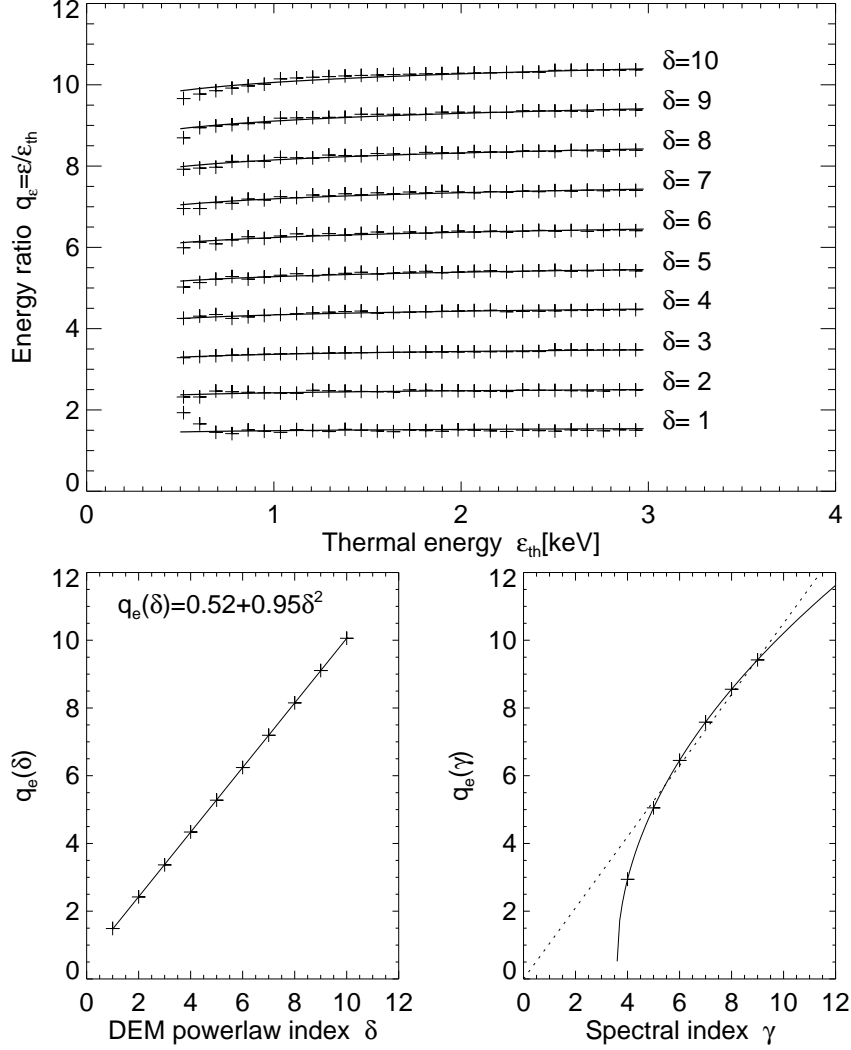


Fig. 3.— Energy ratio $q_e = \epsilon/\epsilon_{th}$ as function of the thermal energy (ϵ_{th}) for various DEM powerlaw indexes $\delta = 1, \dots, 10$ (top panel), the dependence of $q_e(\delta)$ on the DEM powerlaw index δ (bottom left), and of $q_e(\gamma)$ on the photon spectral index γ (bottom right), using the relation $\gamma(\delta)$ shown in Fig. 2.

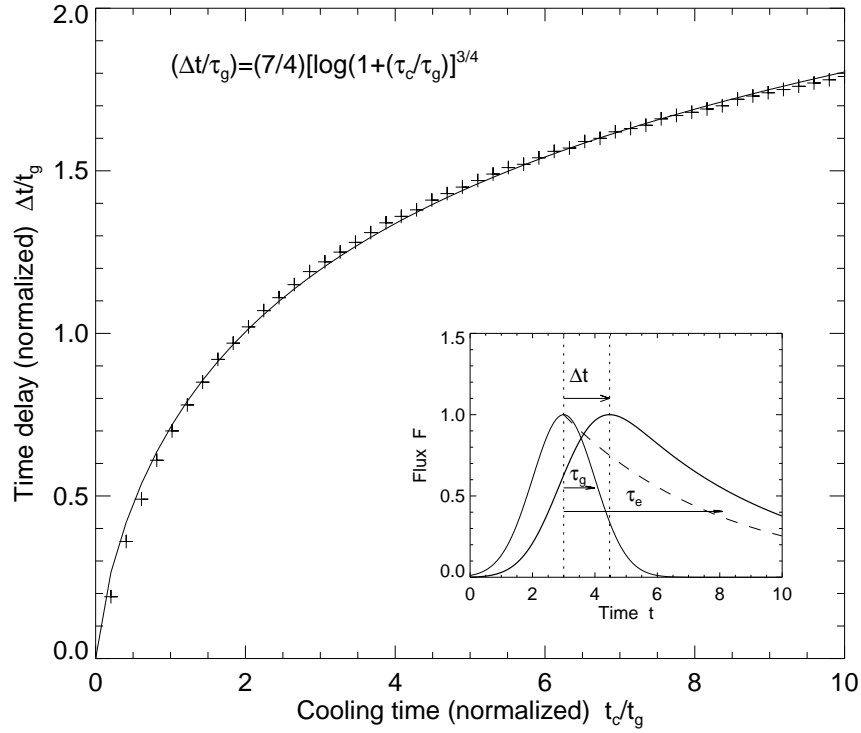


Fig. 4.— Numerically calculated time delays Δt (crosses) of a gaussian time profile with gaussian width τ_g convolved with an e-folding cooling time τ_c . The time scales shown on both axes are normalized by the gaussian time scale τ_g . The functional dependence is approximated with an analytical function (solid curve) given in text (Eq. 20). The agreement between the numerically calculated datapoints and analytical function is $\approx 1\%$.

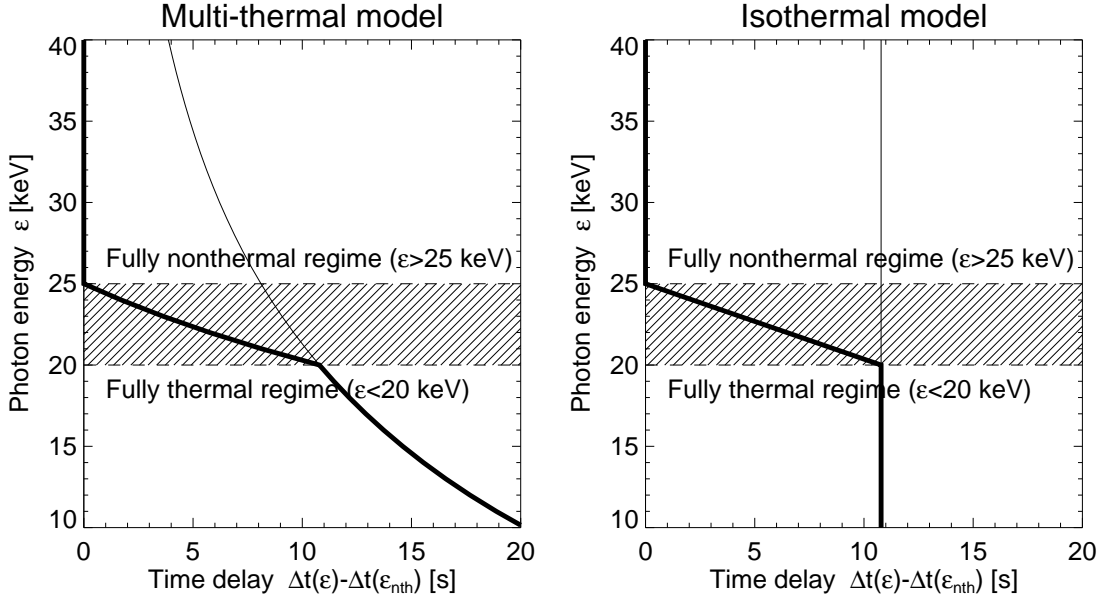


Fig. 5.— Theoretically predicted energy-dependent thermal delays for the multi-thermal model (left) used here and for a hypothetical isothermal model (right). The multi-thermal delays are computed based on conductive cooling times (thick solid curve) for a nonthermal time profile with a Gaussian width of $\tau_g = 10$ s, a flare electron density of 10^{11} cm^{-3} , and a flare loop half length of $L = 10^9$ cm. The pure thermal delay is shown with the thin solid line, while the observable delay (thick curve) is weighted between this pure thermal delay and the zero-delay of the nonthermal component, according to the relative ratio of the thermal and nonthermal fluxes (here assumed to vary linearly from one to zero in the energy range of 20 to 25 keV). - In the isothermal model (right), the delays would be constant in the purely thermal regime, while they increase towards lower energies in the multi-thermal model (left).

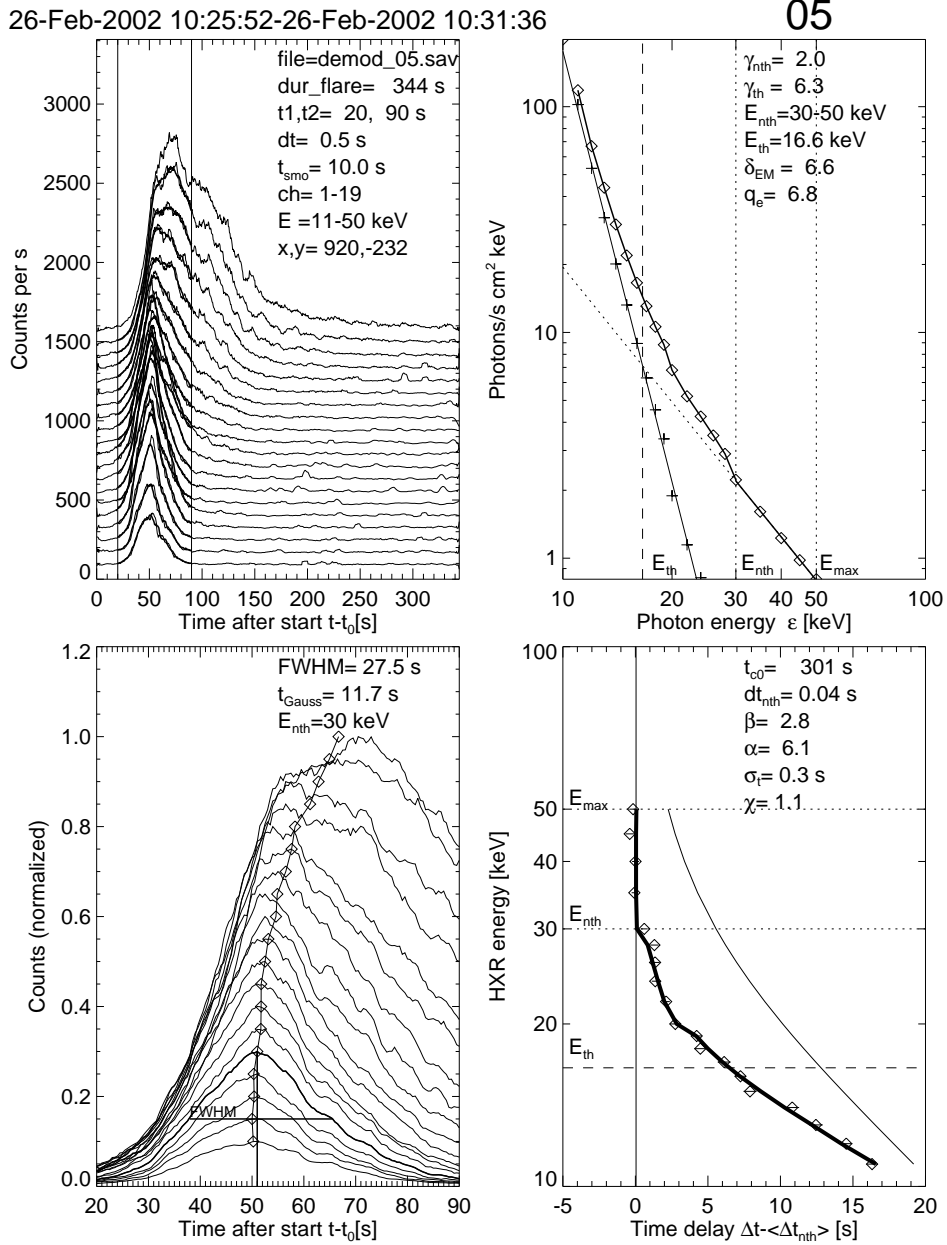


Fig. 6.— *Top left*: Time profiles of 20 energy channels (at $\epsilon = 10, 11, \dots, 20, 22, \dots, 30, 35, \dots, 50$ keV) of the 2002-Feb-26 10:25:52 flare (# 5 in our flare selection list). The time interval $(t - t_0) = 20 - 90$ s after flare start t_0 and energy range of suitable channels are overplotted with smoothed time profile segments in thick line style. *Top right*: The total flux spectrum is shown for the selected time interval (diamond symbols). A nonthermal powerlaw spectrum is fitted in the $\epsilon = 30 - 50$ keV range (dotted line) and subtracted from the total flux spectrum: The remaining thermal spectrum (cross symbols) is also fitted with a powerlaw function (thin line). *Bottom left*: The selected time interval is plotted in an enlarged frame, where the FWHM is measured at the lowest nonthermal energy channel $\epsilon_{nth} = 30$ keV (thick line). The relative cross-correlation delays between the time profiles are marked with diamonds. *Bottom right*: The relative time delays $\Delta t - \langle \Delta t_{nth} \rangle$ are shown (diamonds with error bars) and fitted with the conduction cooling delay model described in text. The pure thermal delay is shown with a thin curve, and the best-fit (thermal/nonthermal-weighted) delays are shown with a thick solid curve. The nonthermal time reference is marked with a vertical thin line.

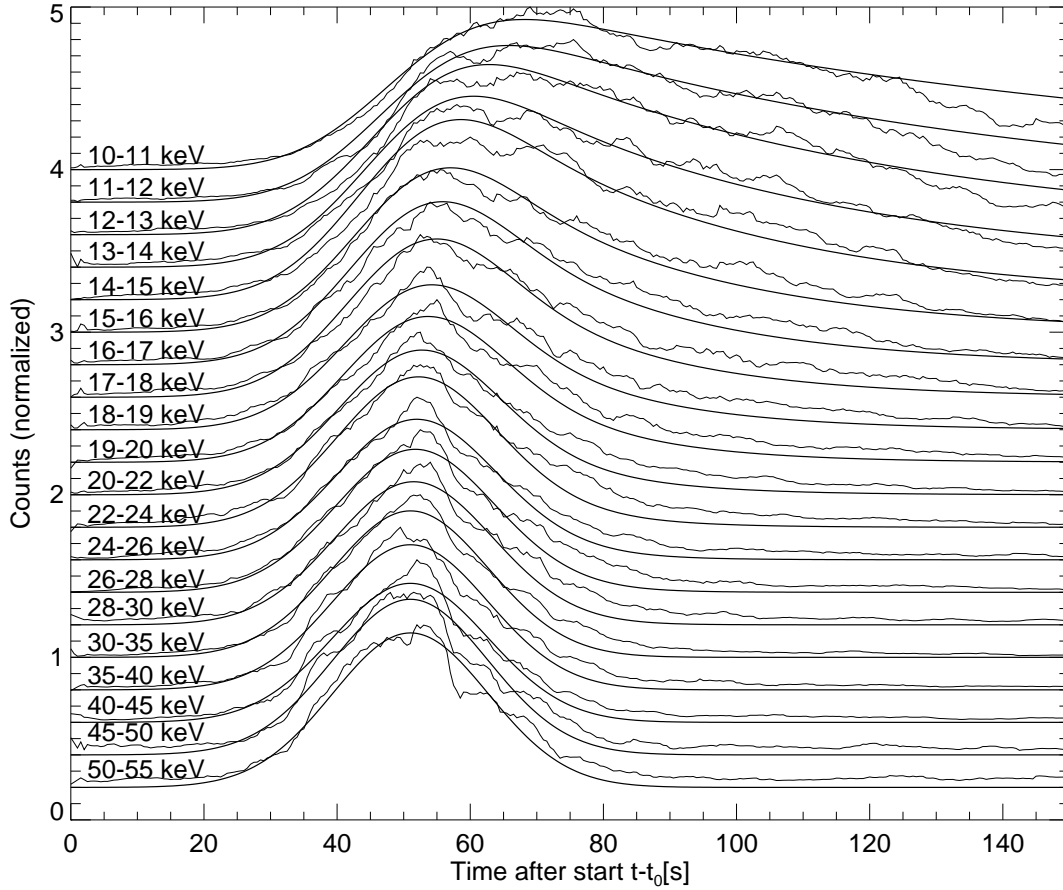


Fig. 7.— Observed (noisy curves) and theoretically predicted time profiles (smooth curves) based on the parameters inferred from the best-fit model (see Fig. 6): Gaussian width of injection profile $t_{gauss} = 11.7$ s, conductive cooling time $t_{c0} = 301$ s (at $T=11.6$ MK or $\epsilon_{th} = 1$ keV), energy ratio $q_e = 6.8$, and weighting factors $w_{th}(\epsilon)$ inferred from thermal/nonthermal flux spectra (see Fig. 6, top right). Note that the e-folding decay time is predicted based on the energy-dependent time delay measurements.

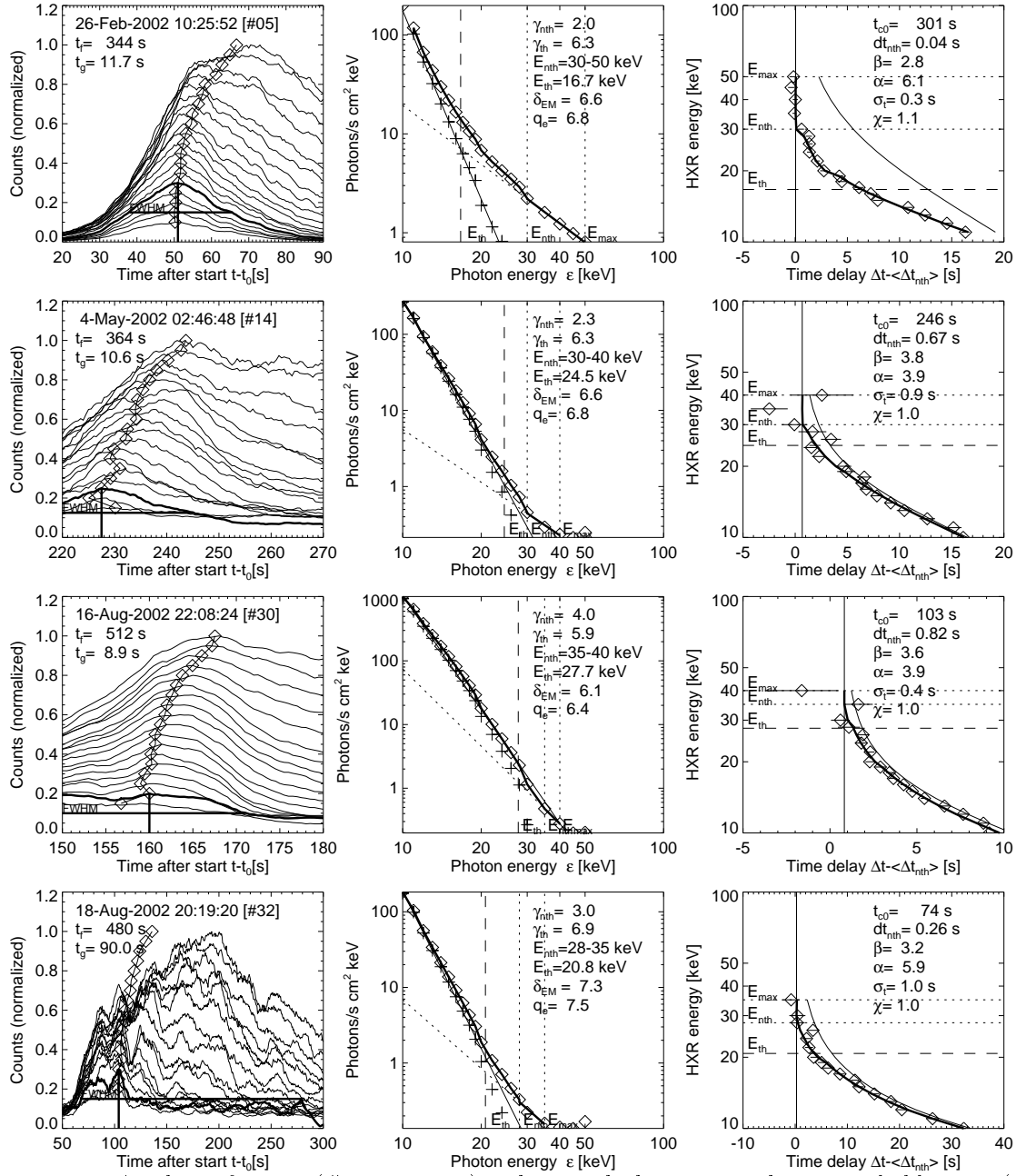


Fig. 8a.— A subset of events (#5, 14, 30, 32) is shown, which represent the most reliable cases (see selection criteria in text). For each case we show the expanded flux time profiles in the time window where they have been cross-correlated to measure the time delays (left panels), the spectral modeling (middle panel), and the energy-dependent time delay measurements with the model fitting (right panels). The representation is identical to Fig. 6).

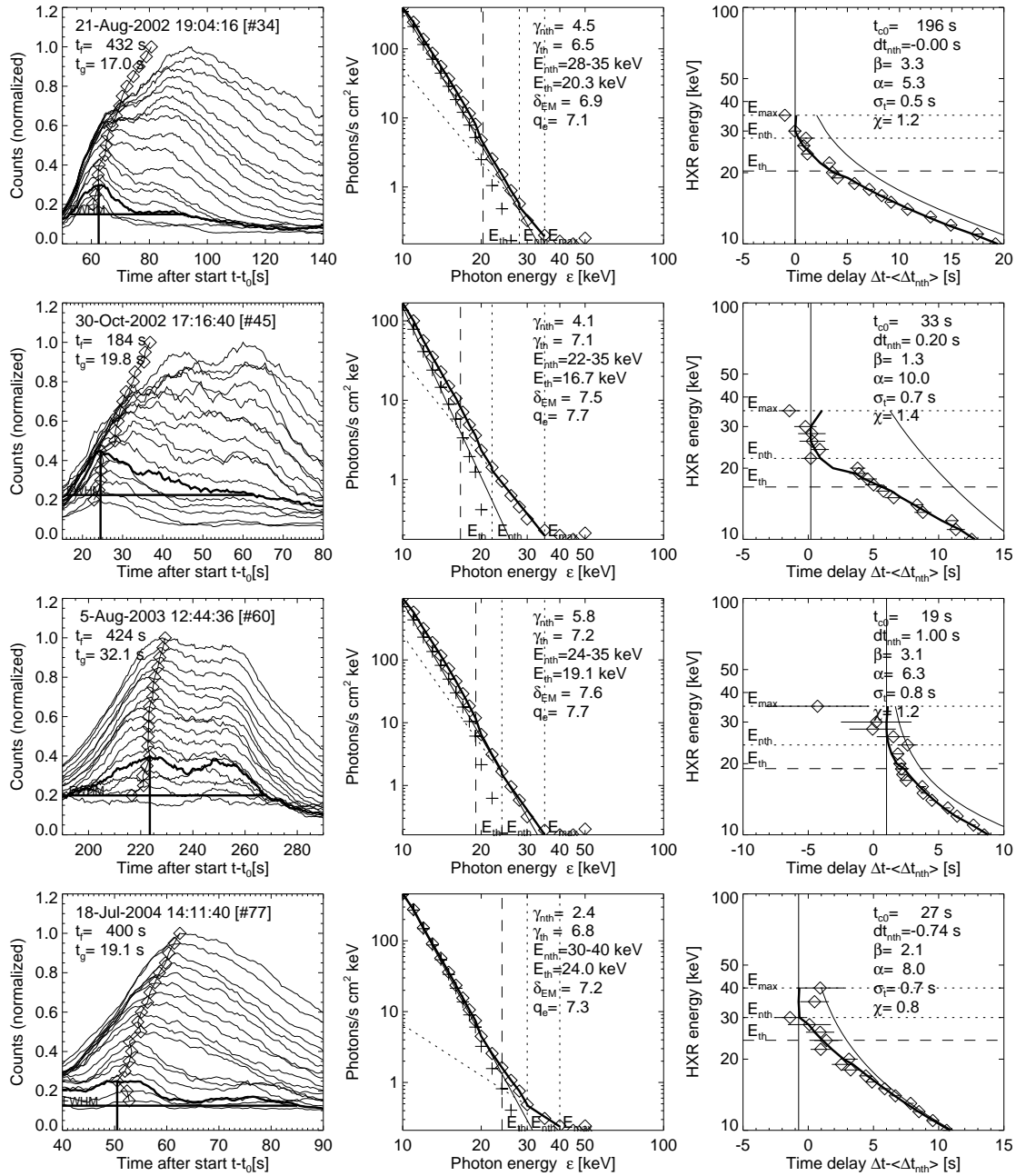


Fig. 8b.— Events #34, 45, 60, 77 - (continued from Fig. 8a)

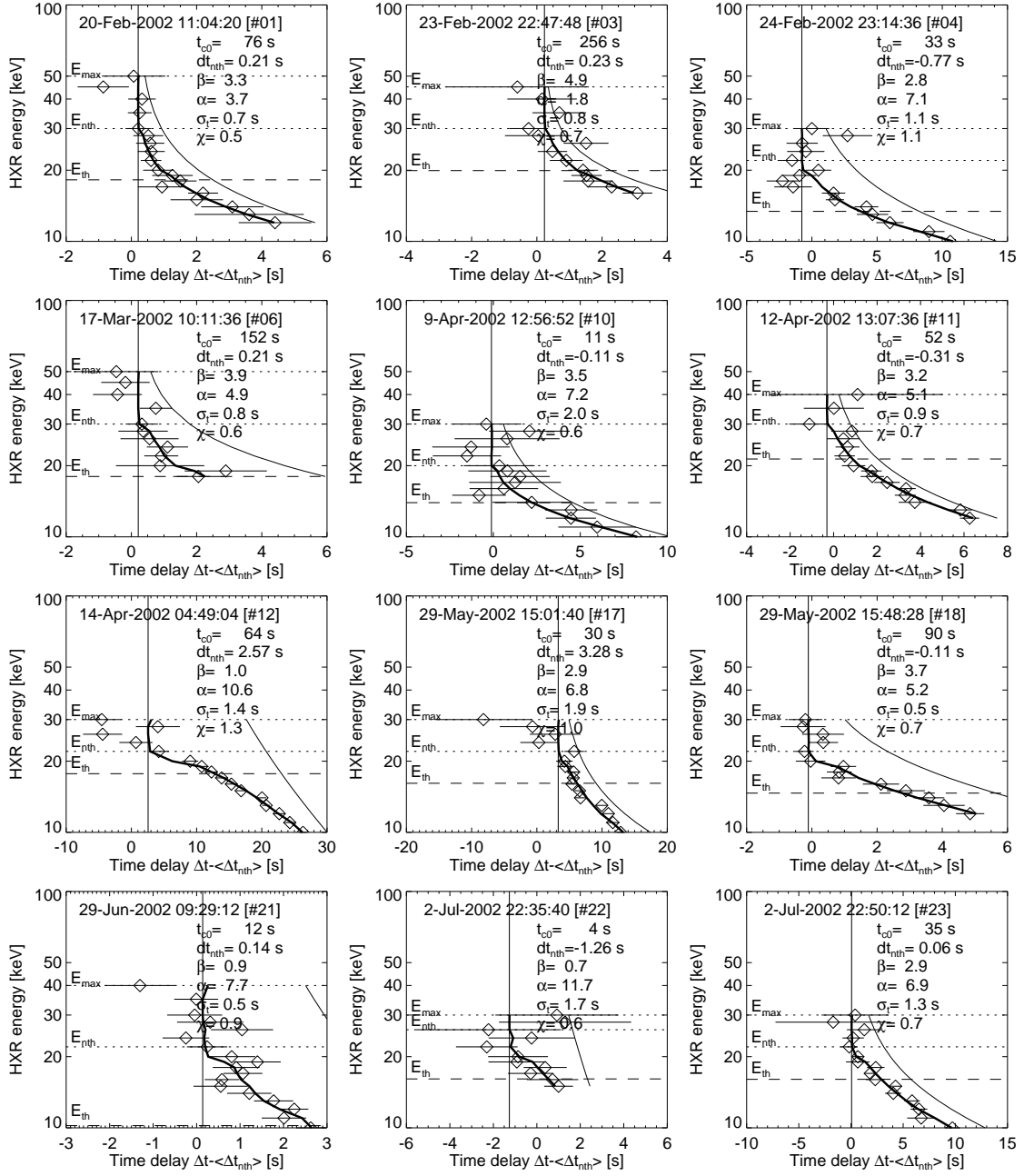


Fig. 9a.— Energy-dependent time delay measurements and model fits of all other events with acceptable fits not shown in Fig. 8 (36 cases).

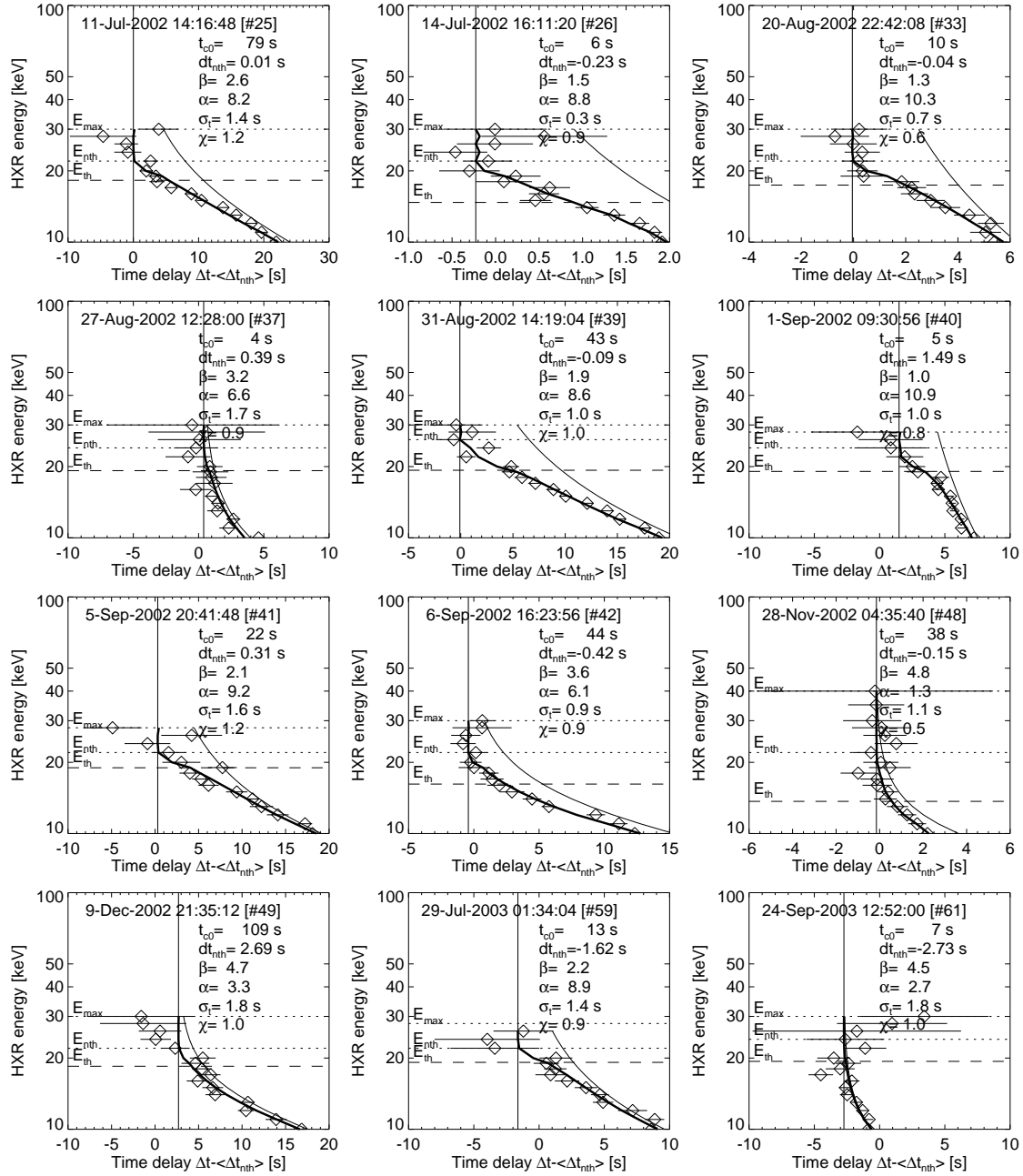


Fig. 9b.— (continued from Fig. 9a)

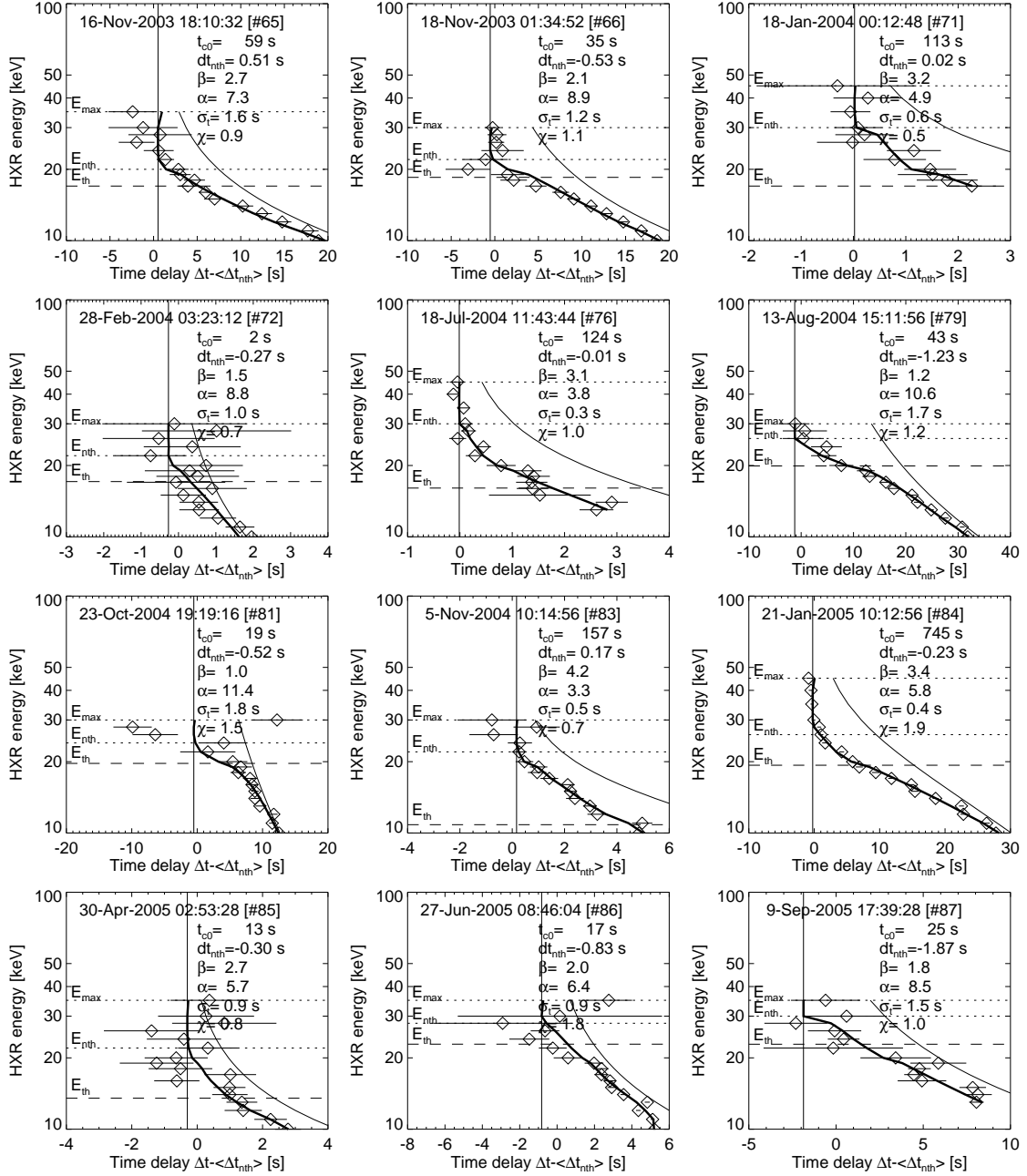


Fig. 9c.— (continued from Fig. 9b)

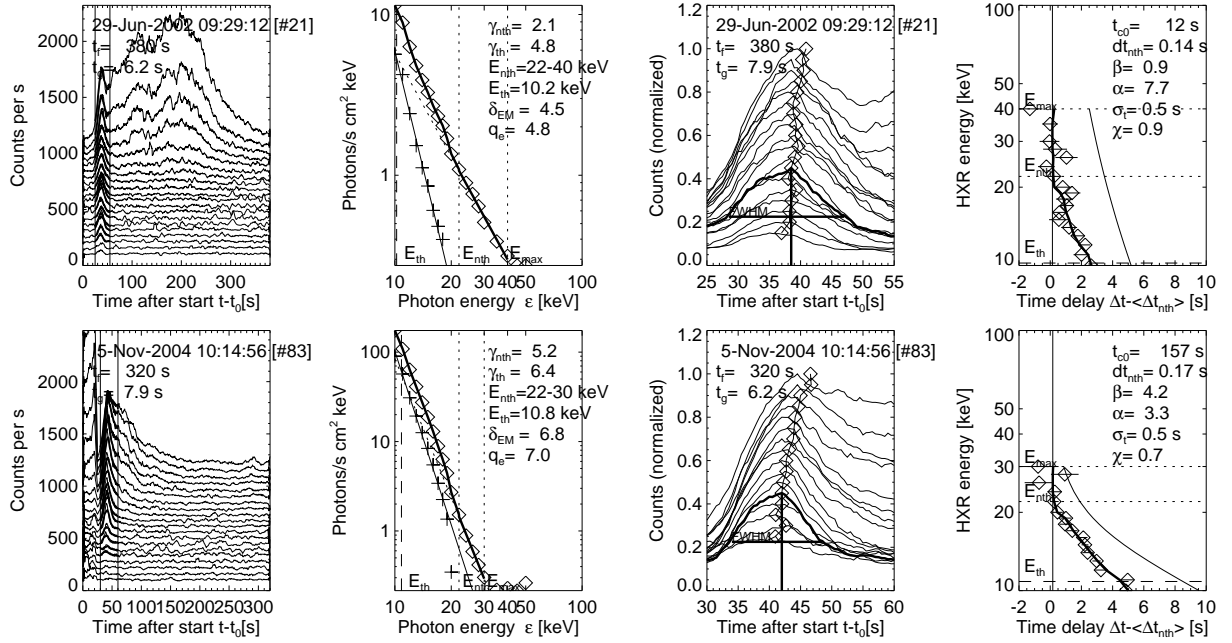


Fig. 10.— Two special events (#21, 83) where the nonthermal emission dominates down to $\epsilon_{th} \approx 10$ keV. Note that in both flares are very impulsive short-duration pulse ($t_g \approx 6 - 8$ s) occurs at the very start of the flares.

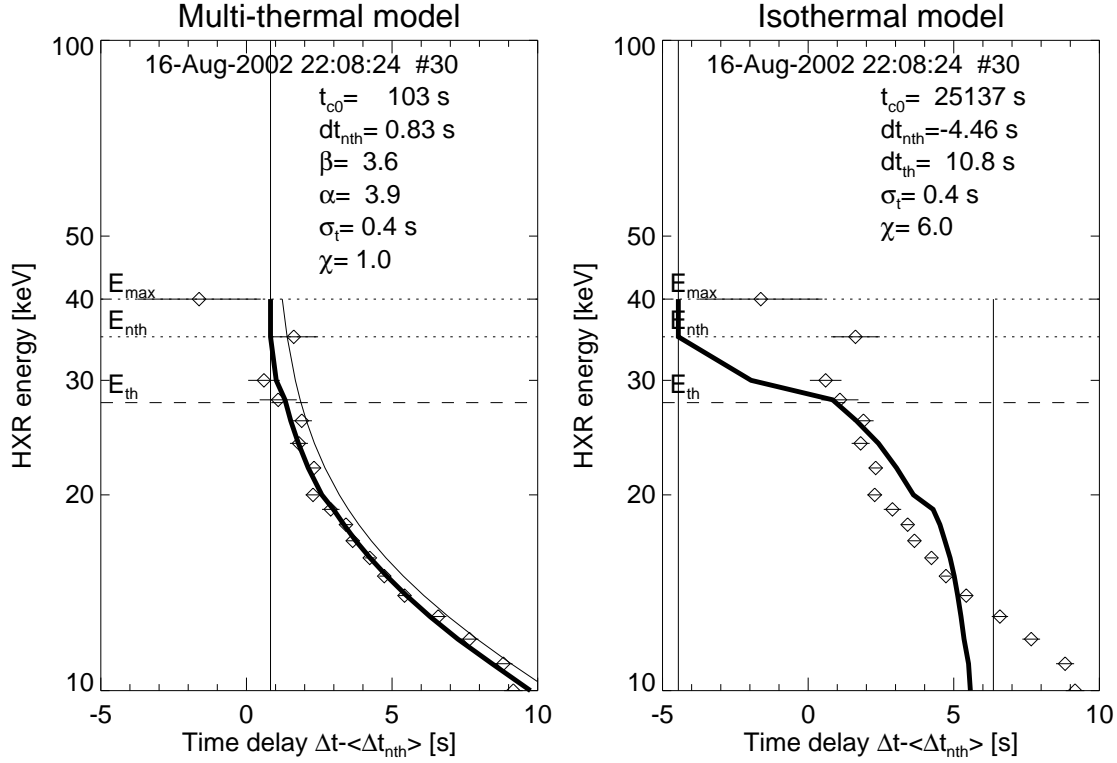


Fig. 11.— Comparison of fitting the multi-thermal model (left) and a hypothetical isothermal model (right) to the flare event #30. Timeprofiles and spectra of this event are shown in Fig. 8a (third row). The two theoretical models are also illustrated in Fig. 5. Note that the main difference between the two models is in the purely thermal energy range, where the predicted delay asymptotically approaches a constant for the thermal model (right), while the delay progressively becomes larger in the multi-thermal model (left). The multi-thermal model is consistent with the data (left, $\chi = 1.0$), while the isothermal model is not (right, $\chi = 6.0$).